A flexible all–solid–state Li–ion battery manufacturable in ambient atmosphere

Shicheng Yu[a,], Qi Xu[a,b], Chih–Long Tsai[a], Marija Hoffmeyer[c], Xin Lu[a,b], Qianli Ma[d], Hermann Tempel[a], Hans Kungl[a], Hans–D. Wiemhöfer[c,e] and Rüdiger–A. Eichel[a,b,e]*

[a]Institut für Energie– und Klimaforschung (IEK–9: Grundlagen der Elektrochemie), Forschungszentrum Jülich, D–52425 Jülich, Germany

[b]Institut für Materialien und Prozesse für elektrochemische Energiespeicher– und wandler, RWTH Aachen University, D–52074 Aachen, Germany

[c]Institut für Anorganische und Analytische Chemie, Westfälische Wilhelms–Universität Münster, D–48149 Münster, Germany

[d]Institut für Energie– und Klimaforschung (IEK–1: Werkstoffsynthese und Herstellungsverfahren), Forschungszentrum Jülich, D–52425 Jülich, Germany

[e]Institut für Energie– und Klimaforschung (IEK–12: Helmholtz–Institute Münster, Ionics in Energy Storage), Forschungszentrum Jülich, D–48149 Münster, Germany

KEYWORDS: flexible all–solid–state Li–ion battery, free–standing electrodes, polymer electrolyte, polyphosphazene, PVDF–HFP, carbon nanotube (CNT), $LiTi_2(PO_4)_3$, $Li_3V_2(PO_4)_3$

ABSTRACT: Rational design and exploration of safe, robust and inexpensive energy storage systems with high flexibility are greatly desired for integrated wearable electronic devices. Herein, a flexible all–solid–state battery possesses competitive electrochemical performance and mechanical stability has been realized by easy manufacture processes using carbon nanotube enhanced phosphate electrodes of $LiTi_2(PO_4)_3$ and $Li_3V_2(PO_4)_3$ and a highly conductive solid

polymer electrolyte made of polyphosphazene/PVDF–HFP/LiBOB. The components were chosen based on their low toxicity, systematic manufacturability and (electro–)chemical matching in order to ensure ambient atmosphere battery assembly and to reach high flexibility, good safety, effective interfacial contacts, and high chemical and mechanical stability for the battery while operation. The high energy density of the electrodes was enabled by a novel design of the self–standing anode and cathode in a way that a large amount of active particles are embedded in the CNT bunches and on the surface of CNT fabric, without binder additive, additional carbon or large metallic current collector. The electrodes showed outstanding performance individually in half–cells with liquid and polymer electrolyte, respectively. The prepared flexible all–solid–state battery exhibited good rate capability that more than half of its theoretical capacity can be delivered even at 1C at 30 °C. Moreover, the capacity retentions are higher than 75% after 200 cycles at different current rates and the battery showed smaller capacity fading after cycling at 50 °C. Furthermore, the promising practical possibilities of the battery concept and fabrication method were demonstrated by a prototype laminated flexible cell.

1. INTRODUCTION

Portable and flexible smart electronics brought great convenience to daily life and become the dominant tendency toward wearable integrated configurations with multifunction.[1–3] To overcome the limited energy storage of this kind of electronic devices, considerable efforts have been dedicated to develop high performance flexible energy storage systems and their integration with functional sensors.[4–6] The energy storage devices contained in integrated configurations are commonly conventional supercapacitors and lithium–ion batteries.[7–10] The former are limited by their low energy density and critical self–discharge,[7,8] and the latter suffer severe safety issues owing to the content of toxic and flammable organic electrolytes.[9,10] To this end, all–solid–state

Li–ion battery, which comprise organic or/and ceramic solid electrolyte instead of liquid one, is one of the most promising replacement due to their wider operable temperature range and inherent high safety, as well as potentially high energy density.[11,12] Thus, it is highly desirable to develop all–solid–state Li–ion batteries with good safety and flexibility, stable output voltage and, ideally, good air–atmosphere manufacturability for powering the wearable smart electronics. Remaining challenges for that are not only at the fabrication of high performance flexible electrode and electrolyte materials but also regarding the crucial interface issues between the components in battery.[13–15]

For the electrodes, metallic Li[16] and Si anodes[17] or widely used layered $LiNi_xMn_yCo_zO_2$ (NMC) cathode class[18] may not be suitable for fabricating batteries for the integration with wearable electronics due to their features of flammable, large volume change during battery operation and containing toxic elements, respectively. NASICON–type anodic $LiTi_2(PO_4)_3$ and cathodic $Li_3V_2(PO_4)_3$ are made of environment friendly materials. In addition, they are constructed by stable lattice structures consisting three dimensional pathways for Li^+ transportation, which enable negligible (de)intercalation strain and fast transportation of Li^+ while cycling, leading to good rate performance and extended cycle life.[11,14] The intrinsically poor electronic conductivity of NASICON–type materials can be mitigated by elemental doping, optimization of particle size or surface modification in terms of carbon coating.[19–22] Regarding the flexibility of electrodes, instead of using large amount of non–conductive binders, the recent research trend is to fabricate electrodes possess high specific energy density and flexibility in novel geometric designs without the application of carbon additives, binder or even conventional metallic current collectors.[23–25] Such an electrode is usually made of active material in combined with graphene or carbon nanotubes (CNT), and feature a high in–plane electrical conductivity, an outstanding tensile

modulus and great mechanical endurance.[26–28] The elastic feature of carbon–based fabrics can also eliminate the influence caused by volume variations of embedded active materials during charge–discharge, and thus preserve the microstructure of electrodes from deformation caused by internal strain.[13] Comparing the application of CNT fabric with graphene in flexible electrodes, advantages of low cost, high flexibility, substrate–free and sufficient content of graphitized carbon make it highly competitive for large scale production. With respect to electrode fabrication, direct formation of active materials on CNT surface usually results in a low mass loading thin electrode.[13] On the other hand, although high loading of active materials can be casted/deposited on the CNT surface, it tend to detach easily during battery operation or under mechanical force in a flexible battery, both leads to serious fading of performance.[29,30] Therefore, for practical applications, developing high mass loading CNT supported NASICON–type electrodes with high flexibility and small active particle size are of great interest in the development of wearable all–solid–state Li–ion battery.

Regarding suitable solid electrolyte for the flexible all–solid–state Li–ion batteries, solid polymers with wide electrochemical stability windows and intrinsic high flexibility is considered to be the best candidate.[31–33] Besides, even without high temperature treatment, external pressure or other complicated interfacial engineering as mostly needed for ceramic electrolyte, sufficient contact areas can be easily generated between polymer electrolyte and electrodes by conventional coating methods. Among the polymer electrolytes, polyphosphazenes grafted with the side chains of oligoethylene oxide exhibited good flexibility and enhanced ionic mobility that are benefited from their complete amorphous property and tremendously low glass transition temperature.[34–36] Furthermore, the outstanding chemical and thermal stabilities of organo–modified polyphosphazenes and the availability of a convenient synthetic route towards high purity

polymers by a living cationic polymerization enable the great potential for practical application of this material in flexible all–solid–state battery.[35–38]

Further, an obligatory precondition for further development in the research area of flexible all–solid–state Li–ion batteries is to overcome interfacial challenges. The origin of (electro–)chemical interfacial issues can be attributed to atomic–level reactions (e.g. elemental inter–diffusion)[39,40] and the formation of space charge layers.[41] Both will lead to the variated interphase and interface conditions, thus result in an increased interfacial resistance. On the other hand, especially for the flexible batteries, effective charge transport may be interrupted by the micro contact issues caused by insufficient solid/solid connection and the formation of cracks.[42] Both (electro–)chemical and mechanical issues can be circumvented by a rational selection of mutually well–matched electrolyte and electrodes materials.[14,43] Specifically, in this work, we demonstrate a flexible, scalable and ambient atmosphere manufacturable all–solid–state battery combining a CNT enhanced electrodes of $LiTi_2(PO_4)_3$ (LTP/CNT) and $Li_3V_2(PO_4)_3$ (LVP/CNT) with a solid polymer electrolyte that made of highly ionic conductive, highly flexible poly[bis(2–(2–methoxyethoxy)ethoxy)phosphazene] (MEEP) and mechanically stable poly(vinylidene fluoride–*co*–hexafluoropropylene) (PVDF–HFP). Both of the electrode and electrolyte materials are less toxic and safe for wearable electronic devices. The choice of electrode materials was constrained to phosphate backbone structures that are expected to be (electro–)chemically stable with the applied solid polymer electrolyte, profiting from the strong P−O bonds. High mass loading of the electrodes is ensured by embedding small active particles in the bulk bunches and on the surface of CNT fabric. The corresponding all–solid–state battery enables good rate performance and cycling life at 30 and 50 °C. In addition to the satisfactory manufacturability and good stability against the oxygen atmosphere of the components, the battery exhibited good flexibility and

superior mechanical stability as were ensured by polymeric features of the electrolyte and elastic nature of CNT fabric.

2. RESULTS AND DISCUSSION

2.1. Structural Analysis of Electrodes

The detailed preparation of electrodes, electrolyte and battery assembly are presented in supporting information. The chemical composition, carbon structure and active mass loading of LTP/CNT and LVP/CNT were analysed by X–ray Diffraction (XRD), Raman spectroscopy and thermogravimetric analysis (TGA) measurements. The obtained results are revealed in Supporting Information, Figure S1 and S2.

As shown in the XRD profiles in Figure S1a–c, no impurity was detected for the electrodes except the additional diffraction peaks at 26° and 44° that arise from CNT fabrics, indicating that phase pure LTP and LVP are obtained in presence of CNT. The structural features of carbon in the CNT, LTP/CNT and LVP/CNT were investigated by Raman spectroscopy as shown in Figure S1d. Three distinguishable Raman bands at 1350 cm^{-1} (D band), 1580 cm^{-1} (G band) with a shoulder around 1605 cm^{-1} and 2690 cm^{-1} (2D band) are observed for pristine CNT, which can be attributed to the disorder–induced features of the CNT, Raman–active, in–plane atomic displacement E2g mode and the overtone of D band.[44] When comparing the Raman spectra of all three samples, the similar G band intensities are suggesting that the highly graphitized carbon kept stable after active material decoration in CNT fabrics. The appearance of the D band at the same wavenumber for all samples indicates the existence of defect sp^3 carbon. Although the P–O Raman vibrations are invisible in the results of electrodes due to the high intensity of carbon bands, recognizable differences between pristine CNT and the self–standing electrodes are that the position of the G

band is shifted to lower wavenumbers in both electrodes. Since the G–band is quite sensitive to doping and minor strains, the shifts are assigned to the increased bond length of the graphite carbon arising from the embedded active materials.[45,46] Moreover, I_D/I_G ratio of CNT, LTP/CNT and LVP/CNT is 0.27, 0.39 and 0.46, respectively. The higher I_D/I_G ratio of LTP/CNT and LVP/CNT indicates more defects were generated within CNT upon the infiltration and crystallization of active electrode materials within the CNT. Besides, amorphous carbon was introduced by the carbonization of oxalic acid during annealing of the electrode green bodies. The formed amorphous carbon on the active particle surface can improve the electron transportation efficiency and enhance the binding of CNT and electrode materials.

According to the TGA results on heating to 700 °C, 31.7 and 33.0 wt% of carbon are removed respectively from LTP/CNT and LVP/CNT electrodes, as shown in Figure S2. Since the LTP and LVP materials have negligible mass changes during TGA measurement in the measured temperature range of 50 to 700 °C, the remaining specimens are a mixture of LTP or LVP with a tiny amount of Fe_2O_3 that is introduced by the Fe catalyst impurities in CNT. The amount of Fe impurity in electrodes, according to the TGA results of CNT fabric, is roughly 0.8 wt%. Hence, the active material mass loading values of 67.5 wt% for LTP/CNT and 66.2 wt% for LVP/CNT are their actual values. On the basis of the TGA result and the total mass of both electrodes, high active loadings of 7.5 and 7.3 mg cm^{-2} for LTP/CNT and LVP/CNT, respectively, have been obtained. These loading values are greater than most of the reports on flexible electrodes,[47–49] thus that the prepared electrodes are capable for the application in high energy density Li–ion batteries. Furthermore, the mass loading of electrodes can be easily controlled by adjusting the ratio of liquid precursor amount to the CNT fabric surface area in the coating process.

The surface morphology features of CNT fabric after washing, as well as the LTP/CNT and LVP/CNT electrode were evaluated by SEM. As shown in Figure S3, the washed CNT composes as a web of curved continuous nanotubes with 20–30 nm diameter. The pore size (>300 nm) in CNT bunches is large enough for embedding the active materials after washing and was well preserved after electrode fabrication that allows the penetration of the polymer electrolyte mixture during coating/casting process. In the surface SEM images of the self–standing LTP/CNT and LVP/CNT electrodes in **Figure 1**a and b, LTP and LVP particles showed a small size around 100 nm, and were homogeneously distributed on the surface of CNT fabric. This morphology guarantees sufficient electronic transportation among the active particles on the surface of CNT fabric.

Decoration of LTP and LVP solely on CNT fabric surface will not guarantee the high active loadings of the electrodes. The electrode particles are also positioned in the bulk of CNT fabrics. Insights on the microstructure features of bulk electrodes were extracted by TEM from which the active particles in between the CNT bunches are visible. As illustrated in **Figure 2**a and c, LTP/CNT and LVP/CNT electrodes display high similarity on the bulk microstructure as the LTP and LVP particles, with particle sizes below 100 nm, uniformly embedded in bulk CNT. The nucleation of active particles inside CNT bunches can be attributed to the applied preparation method. As typically for the Pechini–type sol–gel method, the NASICON precursor colloid has a size below 50 nm in diameter,[50] which is much smaller than the pore size of CNT bunches. During the refluxing of the mixture of CNT and precursor solution, with the help of CNT motion in solution, the small colloids can easily diffuse into the CNT bunches and crystallize during calcination. Additionally, the carbon surrounding LTP and LVP particles, as observed in **Figure 2**b and d, are mostly graphitized carbon, which will positively affect the electronic

transportation of active materials in bulk CNT fabrics. The lattice fringes of LTP and LVP are visible in the high–resolution TEM images indicating their high crystallinity. The CNT in both electrodes act as electronic pathways that interconnect the LTP or LVP particles, providing the electrode with a high electronic conductivity (**Figure 2**e). Upon twisting, rumpling and folding the prepared electrodes, no significant separation of active particles or deterioration in the integrity was observed (**Figure 2**f), indicating good flexibility of the free–standing electrodes and the efficient bonding between CNT and active particles.

The morphology features of the self–standing electrodes are expected to positively influence the electrochemical performance due to the aspects listed in following. (a) The high mass loading electrodes, which are free of non–conductive binder and metallic current collector, could effectively benefit to the total capacity at cell level. (b) The small LTP and LVP particles decorated on the surface and in the bulk of CNT fabrics guarantee the short e^- diffusion pathways of active materials that offers excellent kinetics for lithiation/de–lithiation and lower the polarization during cycling.[50–52] (c) Amorphous carbon formed by the carbonization of raw materials (mainly oxalic acid) on the active particle surface helps overcome the intrinsically low e^- conductivity of phosphate electrode materials and enhance the binding properties between CNT and active particles, thus ensuring the high flexibility of electrodes. (d) The high porosity (~70% for both electrodes, calculated based on the relative and theoretical densities of components) and large specific surface area (61.2 $m^2 g^{-1}$ for LTP/CNT and 64.7 $m^2 g^{-1}$ for LVP/CNT measured by BET) of the electrodes allow the electrolytes easily penetrate into the bulk electrodes and coat on the CNT, thus assure sufficient contact area between electrode and electrolyte. As shown in the bulk and surface SEM images of the electrolyte coated electrode in **Figure 1**c and d, respectively, the bulk CNT bunches and active particles in the electrode are fully covered with solid polymer

electrolyte after the drop coating. Furthermore, the surface of the electrode is completely coated with polymer electrolyte after the tape casting that no pore is visible in the randomly focused area under SEM. In short, the presented LTP/CNT and LVP/CNT electrodes are expected to provide sufficient flexibility, good rate and cycling performance in Li–ion batteries.

2.2. Structural and Electrochemical Analysis of Electrolyte

FT–IR and TEM were carried out for the structural studies of the MEEP/PVDF–HFP/LiBOB solid polymer electrolyte as the results are shown in Figure S4. FT–IR spectrum shows that two main regions of interest were identified: (a) the stretching and oscillating frequency of the carbonyl double bond, C–O, observed in the region 1750–1850 cm^{-1} originating from the LiBOB, and (b) the merged and broadened peaks in the range of 800–1270 cm^{-1} that can be assigned to the representative peaks of the components of PVDF–HFP (amorphous PVDF–HFP, CF_2 and CH_2) and MEEP polymer (P–N, P–O–C, C–O–C and P–N).[53,54] Moreover, the detected tiny peak for crystalline phase PVDF–HFP appears at about 700 cm^{-1} signifying that a certain level of crystallinity of the polymer electrolyte which improves mechanical stability. Combined the FT–IR result with the insert photograph in Figure S4a, in which one can see the homogenous light brown color and the smooth surface of the solid polymer electrolyte, it's can be concluded that the polymer of MEEP and PVDF–HFP are well blended in the structure.

Further observation of the microstructure of the solid polymer electrolyte could help to understand the Li^+ transportation mechanism. In the electrolyte, Li^+ transportation is faster in MEEP due to its low dissociation energy with Li^+ and low crystallinity compared to PVDF–HFP,[35] whereas PVDF–HFP is supposed to serve as the framework for upholding the structure and offers additional pathways for Li^+.[55,56] Hence, a well–mixed MEEP, PVDF–HFP and lithium salt is desirable in order to achieve a stable solid structure with high Li^+ conductivity. As shown in the

low–magnification TEM image (upper image in Figure S4b), the black dots are folded MEEP polymer since the atomic masses of phosphorus and nitrogen are larger than carbon. Nano–sized BOB anions are uniformly distributed in the polymer as can be seen in the high magnification TEM image (bottom image in Figure S4b). The homogenously mixed MEEP and lithium salt in PVDF–HFP could decrease the crystallinity of polymer and hence boost segmental motion for Li^+ migration.

The ionic conductivity of the solid polymer electrolyte (thickness = ~175 µm, ∅ = 12 mm) at –30 to 100 °C was determined by fitting Nyquist plots of the impedance spectra, as displayed in **Figure 3**a. The equivalent circuit is revealed as an inset of **Figure 3**a, where *R* and CPE attributed to the resistance and constant phase element, respectively. As the capacitance values of CPE1 and CPE fit to the characteristic capacitance from the contribution of the polymer and the interface between electrolyte and blocking electrodes respectively, the *R* is attributed to the polymer bulk resistance which strongly depends on the measured temperature.

Figure3b shows Arrhenius plot of the MEEP/PVDF–HFP/LiBOB electrolyte that compared the conductivity and temperature dependence. The observed non–linear behavior of Arrhenius plot is typical for polymer electrolytes that can be defined by the VTF equation and ascribed to the strong interaction between the polymer segmental relaxation and ionic motion,[57–59] which implies that the motions of polymer segment and mobile ions are well coupled. Increasing the temperature from –30 to 100 °C results in ion conduction jump up to five orders of magnitude, i.e., from 10^{-8} to 10^{-3} S cm^{-1}, and high conductivity values are achieved at room temperatures and above, i.e., 1.32×10^{-4} S cm^{-1} at 30 °C, indicating the suitability of the electrolyte for practical application in all–solid–state Li–ion batteries.

The electrochemical stability window of solid polymer electrolyte was studied by CV measurement with a scan rate of 1 mV s^{-1} at 30 °C. As demonstrated in **Figure 3**c, at potentials above 4.7 V, the oligoether side chains in the polyphosphazene starts oxidative degradation. At around 0 V, the reversible deposition and dissolution of lithium with Cu electrode can be observed. Hence, the solid polymer electrolyte is electrochemically stable within the voltage range of 0–4.7 V, which is larger than most of the intrinsic electrochemical windows of ceramic electrolytes.[31] Based on the results, the MEEP/PVDF–HFP/LiBOB polymer electrolyte is suitable for Li–ion batteries using the high–potential electrode materials, such as $Li_3V_2(PO_4)_3$.

2.3. Electrochemical Performance of Batteries

2.3.1. Performance of half–cells with liquid and polymer electrolyte

Metallic Li anode is not the best option for the all–solid–state batteries that will be integrated with wearable electronic devices due to safety concerns. Whereas it can be used to assess the electrochemical property of the individual electrodes and polymer electrolyte prepared in this work before assembly of the flexible all–solid–state batteries. For this purpose, half–cells with liquid as well as polymer electrolyte were prepared and tested in the potential ranges of 1.5–3.5 V (*vs* Li/Li^+) for LTP/CNT and 3.0–4.3 V (*vs* Li/Li^+) for LVP/CNT, as the results are shown in **Figure 4**.

Figure 4a and b show the first and fifth charge–discharge profiles of the half–cells at a low current density of 0.05C. It can be seen that the Coulombic efficiency of the initial cycle is in the range of 98.2–98.9% for both electrodes in liquid and polymer electrolyte cells, and further increased to more than 99% after five cycles, indicating good reversibility of lithiation/delithiation in the electrodes after initial irreversibility passivation. As shown in **Figure 4**a, the obtained specific discharge capacity of the LTP/CNT half–cell with liquid electrolyte is about 133.8 mAh g^{-1}, corresponding to 97.0% of its theoretical capacity (138 mAh g^{-1}) based on the weight of LTP.

The charge–discharge potential plateau is about 2.5 V that is in good agreement with previous reports.[51,60,61] Since no metal current collector or non–conductive binder is introduced to the electrode, the specific capacity based on the total weight of LTP/CNT electrode reached an high value of 100.5 mAh g^{-1}. As shown in **Figure 4**b, in the case of the LVP/CNT half–cell with liquid electrolyte, reversible charge and discharge potential plateaus are revealed at around 4.05 V, 3.65 V and 3.56 V, respectively, corresponding to a sequence of phase transitions of $Li_xV_2(PO_4)_3$ where x = 1.0, 2.0, 2.5 and 3.[52,62] The specific discharge capacities of the cell calculated basing on the loading mass of LVP is 124.8 mAh g^{-1}, corresponding to 93.8% of its theoretical capacity, and 94.2 mAh g^{-1} basing on the total weight of the electrode. The high capacity based on electrode weight demonstrating a promising application prospect of the prepared LTP/CNT and LVP/CNT for high energy density Li–ion battery.

On the other hand, although the LTP/CNT and LVP/CNT half–cells with polymer electrolyte show good capacity retention and high Coulombic efficiency, when comparing the results of these cells with the ones consisting liquid electrolyte, recognizable differences are the decayed capacities, decreased about 20% of the capacities for both electrodes with polymer electrolyte, and stronger polarization as evidenced by the tilted potential plateaus and the large overpotential, or say enlarged plateau potential difference (ΔV). The lower capacity and larger polarization of the cells with polymer electrolyte can be attributed to the sluggish diffusion kinetics at the solid/solid interfaces and the high electrolyte resistance in the all–solid–state batteries compared to the cells with liquid electrolyte. Especially for the LVP/CNT electrode, the potential plateaus of 3.65 V and 3.56 V as were seen for the liquid electrolyte cell are merged and barely be distinguished for the cells with solid polymer electrolyte. Meanwhile, the delivered discharge capacities for the phase transition of $Li_2V_2(PO_4)_3 \leftrightarrow Li_3V_2(PO_4)_3$ are very close in cells with different electrolyte

(corresponding to the plateau potentials between 3.55 V–3.65 V for liquid electrolyte cell and between 3.35 V–3.55 V for polymer electrolyte cell). Likely, the comparably low capacity of LVP/CNT in polymer electrolyte cells is mainly caused by the limited diffusion kinetic of Li^+ between LVP and polymer at high potential around 4.0 V vs Li/Li^+, correlating to the incomplete phase transition of $LiV_2(PO_4)_3 \leftrightarrow Li_2V_2(PO_4)_3$.

Even though, as shown in **Figure 4**a and b, the specific capacities of both solid electrolyte half–cells at 30 °C are close to 80% of their theoretical capacities, respectively, indicating the sufficient electrolyte/electrode connections and effective ion exchange between the electrode and solid polymer electrolyte. It's worth to mention here that the CNT in the electrodes has no contribution to the charge–discharge capacity as the Li^+ intercalation into graphitized carbon takes place at potential below 0.5 V *vs* Li/Li^+ (close to 0.1 V). [63,64]

The impedance changes before and after the five cycles at 0.05C of the half–cells mentioned above were investigated by EIS in the frequency range of 3.0 MHz to 0.1 Hz. As demonstrated in **Figure 4**c, Nyquist plots of all the prepared cells revealed a semicircle in the high frequency region that can be attributed to the charge–transfer processes of the Li^+ through the interface from the surface of the active particles to the electrolyte. The straight lines in the low frequency region are ascribed to the diffusion of Li^+ in the bulk of the electrodes. The cells with polymer electrolyte exhibited stretched semicircles that could be attributed to the space charge layer influenced diffusion processes through the solid/solid interface which is also overlapped with the Li^+ diffusion process in polymer electrolyte. Unfortunately, the polymer resistance and the interface resistance are not possible to be separated from the results. Higher charge–transfer resistances were found for the cells with polymer electrolyte compared with the liquid electrolyte cells due to the high intrinsic resistance of polymer electrolyte and the solid/solid interface connection. The overall

charge–transfer resistances of all the cells slightly decreased after the five cycles that can be possibly attributed to the battery activation process. Upon the initial cycles, irreversible reorganization of Li^+ distribution in the battery normally results in a higher overall conductivity. The low resistance values of all the cells indicate satisfactory electrode/electrolyte interconnections and effective electron/ion transportation in the electrodes.

The rate performance of the half–cells at 30 °C was studied for the subsequent cycles from 0.05C up to 10C as the results are shown in **Figure 4**d. Along with increasing current rates, all the cells showed stable capacities at each state. When the charge and discharge rate was again decreased to 0.1C, almost 100% of their initial capacities can be delivered. For the liquid electrolyte cells, with the current rate increasing to 10C, both of the electrodes were still capable to deliver higher than 90% of their theoretical capacities. Overall, these results of outstanding rate performance indicating the advantages of NASICON–type electrodes with the enhancement of CNT. The rate performance of cells with polymer electrolyte were hindered by the large resistances of polymer and polymer/electrode interface. As shown in **Figure 4**d, owing to the kinetic limitation of Li^+ transport in polymer electrolyte, the discharge capacity decreased severely with increasing of the current rate, only about 70% of their theoretical capacities that can be delivered at 0.5C.

The long–term cycling performances of the LTP/CNT and LVP/CNT half–cells with liquid or polymer electrolyte, respectively, at the current rate of 0.1C are shown in **Figure 4**e. All the cells were stably cycled up to 200 cycles. After 200 cycles, the LTP/CNT half–cell with liquid electrolyte delivered 130.1 mAh g^{-1} with a capacity retention of 96.2% and the LVP/CNT half–cell delivered 116.0 mAh g^{-1} with a capacity retention of 94.3%, which illustrates that the prepared LTP/CNT and LVP/CNT electrodes possess high electrochemical and structural stabilities for a

long–term lithiation/delithiation in the relevant voltage ranges. Both polymer electrolyte cells are almost as stable as for that of the liquid electrolyte ones while slightly lower capacity retention was found for the LVP/CNT cell.

The large capacity based on the total weight of the electrode, high rate performance and long cycling life of the self–standing electrodes in half–cells with liquid electrolyte are benefited from their novel microstructure of active particles in/on the CNT, as well as the stable crystal framework of NASICON–type materials.[13,65] The outstanding electrochemical performance of the half–cells of LTP/CNT and LVP/CNT with polymer electrolyte is indicating high chemical, electrochemical and mechanical compatibilities of the electrodes individually with the polymer electrolyte, especially at the interface.

2.3.2. Performance of full cells with polymer electrolyte

All–solid–state cells were prepared using LTP/CNT as the anode, LVP/CNT as the cathode and MEEP/PVDF–HFP/LiBOB as the solid polymer electrolyte. The choice of the NASICON electrodes is originally based on the considerations of their low toxicity, low volume change during cycling, good air stability, and good compatibility with each other, as well as with the polymer electrolyte. As schematically shown in **Figure 1**, all steps of the battery assembly process including drop coating and tape casting of the electrolyte were performed in normal laboratory conditions in ambient atmosphere, except the final sealing of the cells which was made in the glovebox. Specifically, drop coating of 45 μL/cm^2 polymer electrolyte mixture solution was performed on the prepared LTP/CNT and LVP/CNT electrode surfaces in order to let the polymer electrolyte penetrate into the pores of electrodes to form effective ion conductive pathways in bulk electrodes. The drop coated electrolyte was stabilized at room temperature overnight, dried at 50 °C for 24 hours, and further dried under vacuum at 80 °C for one day. The electrode

morphology after drop coating can be seen in the SEM image in **Figure 1**c. All the CNT bunches and the surface electrode particles are coated with polymer electrolytes while a small amount of remaining pores are observed. After that, 35.5 μL/cm^2 polymer electrolyte solution was tape casted on top of the drop coated electrodes and dried again by following the previous drying process. The electrode surface, therefore, is completely covered with polymer electrolyte as can be seen in the SEM image in **Figure 1**d. The thickness of the tape casted solid polymer electrolyte is about 60 μm on each electrode after drying. The flexible all–solid–state Li–ion batteries were prepared by wetting the coated electrolyte surface by a tiny amount of acetone and simply attaching the electrolyte coated LTP/CNT and LVP/CNT together and hot press the cells at 100 °C with a fixed distance of 350 μm by an electric hot rolling press. Finally, the cells were stabilized at room temperature overnight and further dried under vacuum at 80 °C for 24 hours before they were cut into desired sizes and were sealed in Swagelok–type cells (diameter = 12 mm) or in the plastic sealing film by an office lamination machine, respectively. The electrochemical performances of the cells were evaluated in Swagelok cells in the voltage range of 0.5–2.2 V at 30 °C and 50 °C in order to take advantage of the improved ionic conductivity of polymer electrolyte at a higher temperature, as the results are shown in **Figure 5**. The LTP/CNT and LVP/CNT electrodes were composed with balancing their capacity ratio to1:1.1 in the cell, thus, the specific capacity of the cells is indicated based on the weight of active materials in the anode, the total weight of the anode or the total weight of the two electrodes.

The rate performance and relevant charge–discharge profiles of LTP/CNT|MEEP/PVDF–HFP/LiBOB|LVP/CNT all–solid–state Li–ion battery, cycled with current rates from 0.05C up to 10C for five cycles at each state in the voltage range of 0.5–2.2 V at 30 °C and 50 °C, respectively, are shown in **Figure 5**a–c. At 30 °C, in low current rates (<1C), the battery delivered reasonable

capacity and exhibited low polarization and high overall Coulombic efficiency that can be ascribed to the satisfactory ionic conductivity of polymer electrolyte and the favorable electrolyte/electrode interfacial properties. When the current rate is higher than 1C, the discharge capacities faded dramatically, indicating the kinetic limitation of Li^+ transport in polymer impeding the battery performance. Furthermore, overpotential increases radically in combine with sharply fading of capacity with increasing the current rate, as shown in **Figure 5**b, indicating that the polarization considerably influences the electrochemical behavior of the battery. Nevertheless, when the current rate was down back to 0.1C after cycling at higher rates, as much as the initial discharge capacity can be still delivered due to the good durability of the polymer electrolyte under high overpotential. For the cells cycled at 50 °C degree, the specific discharge capacities are higher than the results obtained at 30 °C at correlated current rates, due to the faster Li^+ diffusion rate and the lower internal resistance of the cells at a higher temperature.[66] As an evidence, the discharge capacity reaches half of its theoretical value with small overpotential even at 3C. Besides, more than a quarter of its initial capacity can be delivered at an extreme high current rate of 10C. As shown in **Figure 5**c, the decrease of discharge plateau at high current rates can be attributed to the ohmic and electrochemical polarizations of the components in the cell, and also the kinetics limited by ion diffusion within the electrolyte and/or at the electrode/electrolyte interfaces.[14,67] Moreover, benefited by the high mass loading of the electrodes, the discharge capacity based on the total weight of anode and both electrodes is 83 and 41 mAh g^{-1}, respectively, even at 30 °C. Cycling tests of the full cells were performed at current rates of 0.1C, 0.5C and 1C at temperatures of 30 °C and 50 °C, respectively, as the results are shown in **Figure 5**d. At 30 °C, the battery exhibited capacity retentions of 91.4%, 84.6% and 75.1% over 200 cycles at 0.1C, 0.5C and 1C, respectively. Interestingly, unlike conventional Li–ion batteries with liquid electrolytes that show faster capacity

fading at higher temperatures,[66,68,69] at 50 °C, capacity retentions are comparably higher at each relevant current rate for the prepared flexible all–solid–state battery. Especially at 1C, capacity retention reached 86.6%, which is 11.5% higher than that for the cell measured at 30 °C. Most of the temperature effects are related to (electro–)chemical reactions taking place between the battery components. Regarding chemical reactions, for instance, the formation and growth of the SEI layer, the relationship between the reaction temperature and rate of chemical reactions follows the Arrhenius equation. Variation of temperature can cause the deviation of electrochemical reaction rate in batteries.[70] Apart from chemical reactions, the ionic and electronic conductivities of components are also affected by temperature. Such as the ionic conductivity of polymer electrolytes used in this work increased about an order of magnitude when the temperature raised from 30 to 50 °C (cf. **Figure 3**b). Rational increasing the operating temperature while remaining below the decomposition temperature of the polymer electrolyte will not significantly accelerate the side reactions between the solid components but rather promotes the wetting of the polymer electrolyte on electrode and accelerates the Li^+ diffusion in the all–solid–state battery as the crystallinity of polymer is decreased. The superior rate performance and long–term cycling ability of the flexible all–solid–state battery are consistent with the results obtained from half–cells, as they benefit from the soft polymer electrolyte, novel morphology of electrodes and stable interface structure of electrode and electrolyte.

2.3.3. Performance of flexible all–solid–state Li–ion laminated cell

The above results have shown the sufficient rate performance and long lifespan of the flexible all–solid–state battery concept, aspect of flexibility was further tested concerning its practical applications. For that, a prototype laminated cell is prepared (cf. **Figure 6**). The sizes of the electrodes are 7.0 cm × 4 cm (LTP/CNT anode) and 7.5 cm × 4 cm (LVP/CNT cathode) with

the same thickness of 120 μm. The theoretical cell capacity is about 29 mAh. Small piece of Al and Cu tapes were used as external contact tabs to provide the current flow, respectively, to cathode and anode. The polymer electrolyte has been filled in the pores in both electrodes by drop coating and was subsequently coated on the surface of the electrodes by tape casting as illustrated in **Figure 1**. After slowly drying and hot pressing, the cell was laminated in plastic sealing film. As shown in **Figure 6**a and b, the cell was initially cycled five times at a low current density of 0.05 mA cm^{-2} (~0.05C) and further cycled fifty times with a larger current density of 0.1 mA cm^{-2} in the voltage range of 0.5–2.2 V at 30 °C. It is worth mentioning that the low efficiency of first cycle could due to the use of plastic sealing film, which allows some oxygen penetration under ambient atmosphere. For a typical pouch cell film, it is known that an Al film is laminated in between two plastic films to stop oxygen penetration. Therefore, the extra oxygen within the cell could cause side–reaction until a SEI was formed to stop further reactions. Nevertheless, the cell exhibited almost 100% cycling efficiency throughout the rest of cycling indicating that the irreversibility of the cell is not related to continuous structural changes or side reactions of the components induced by cycling. Besides, the cell exhibits more tilted charge–discharge voltage plateaus and larger polarizations comparing with the results obtained from Swagelok cells with the battery in a smaller size. The total cell capacities are around 21 mAh, corresponding to 72.4% of theoretical capacity, and were kept stable over 50 cycles. Moreover, as shown in the insert photograph in **Figure 6**a, no layer separation or gas release is visible for the battery after all the cycles. The prototype laminated cell exhibited good capacity retention under static bending conditions, as shown in **Figure 6**c. The charge–discharge curves are well–matched when the cell was bent at different angles or completely folded. The red light–emitting diode indicator was lit up by using two of the prepared laminated batteries connected in series after cutting and rolling,

as shown in **Figure 6**d. At both conditions, the LED remains light even one of the batteries was cut and exposed to air. Based on these results, it can be concluded that the flexibility of the electrolyte and electrodes be inherited to the laminated battery and the material combination is highly safe and stable against mechanical destruction and in ambient atmosphere.

3. CONCLUSION

In summary, a flexible all–solid–state Li–ion battery with polyphosphazene based solid polymer electrolyte and free–standing LTP/CNT and LVP/CNT electrodes has been prepared. These electrodes possess high mass loading, small active particle size, large porosity and pore size for polymer electrolyte penetration during battery fabrication, and can be directly applied to fabricate Li–ion batteries without the application of metallic current collector, electrochemically inactive binder and additive carbon as in the traditional process of electrode manufacturing. CNT in the electrodes mainly serve as a three dimensional network for the electronic conduction and as a flexible host accommodating the active particles. Thanks to the good castability and flexibility of the polymer electrolyte, the bulk and surface of the electrodes can be homogeneously coated with polymer electrolytes and the full battery can be assembled easily by a hot rolling press. High electrochemical performances of the flexible all–solid–state Li–ion battery were achieved even at ambient temperature benefited from the outstanding properties of the electrodes and electrolyte, as well as from the good chemical, electrochemical and mechanical compatibilities of phosphate components. The Swagelok–type all–solid–state Li–ion battery, $LiTi_2(PO_4)_3$/CNT|MEEP/PVDF–HFP/LiBOB polymer electrolyte|$Li_3V_2(PO_4)_3$/CNT, can be cycled for at least 200 cycles at the current rate up to 1C at 30 °C and 50 °C with low capacity fading. Even at 1C, the initial capacity of the battery is more than half of its theoretical capacity. Besides, good electrochemical performances, high flexibility, mechanical safety and air/moisture stability were demonstrated for

the battery concept in prototype flexible laminated cells. Although the output voltage of the full cell is limited by the application of high voltage $LiTi_2(PO_4)_3$ anode, the system is suitable up to certain level for the safely integration with wearable electronics. Moreover, the easy and scalable fabrication process of components and battery assembly (even in air–atmosphere) demonstrated in this work can be easily applied to prepare other kinds of self–standing electrodes with controllable active mass loading, as well as relevant flexible solid–state batteries with a suitable polymer electrolyte. Further tuning the electrodes and electrolyte to improve the output voltage and room temperature rate performance are still under investigation to pave the way for its large–scale practical applications.

ASSOCIATED CONTENT

Supporting Information The Supporting Information is available free of charge on the ACS Publications website or from the author.

Experimental Section and Figure S1–S4. XRD, Raman, TGA of CNT, $LiTi_2(PO_4)_3$/CNT and $Li_3V_2(PO_4)_3$/CNT. SEM images of CNT after washing by HCl and ethanol/water 1:1 (vol./vol.) mixture. FT–IR spectra, photograph and TEM images of the prepared MEEP/PVDF–HFP/LiBOB solid polymer electrolyte.

AUTHOR INFORMATION

Corresponding Author

*E–mail: s.yu@fz–juelich.de

ORCID

Shicheng Yu 0000–0002–6619–3330

Chih–Long Tsai 0000–0001–8103–3514

Xin Lu 0000–0002–6631–7532

Qianli Ma 0000–0002–4709–4927

Hermann Tempel 0000–0002–9794–6403

Hans Kungl 0000–0003–3142–3906

Hans–D. Wiemhöfer 0000–0002–6049–9953

Rüdiger–A. Eichel 0000–0002–0013–6325

Author Contributions

All authors made contributions to manuscript preparation and have given final approval for publication.

Notes

The authors declare no competing financial interest.

ACKNOWLEDGMENTS

This work was financially supported by the projects of "Materials and Components to Meet High Energy Density Batteries III" of the funding program "Excellent battery" from the Bundesministerium für Bildung und Forschung (BMBF) (Project No.: 13XP0258B). The carbon nanotube fabrics were supplied by Tortech Nano–Fibers Ltd. (Israel) free of charge, for which the authors are grateful. S. Yu is grateful to Daniel Kröger, who helped with TEM experiments.

REFERENCES

(1) Zhu, M.; Huang, Y.; Huang, Y.; Pei, Z.; Xue, Q.; Li, H.; Geng, H.; Zhi, C. Capacitance Enhancement in a Semiconductor Nanostructure–Based Supercapacitor by Solar Light and a Self–Powered Supercapacitor–Photodetector System. *Adv. Funct. Mater.* **2016**, *26*, 4481–4490.

(2) Chen, C.; Cao, J.; Wang, X.; Lu, Q.; Han, M.; Wang, Q.; Dai, H.; Niu, Z.; Chen, J.; Xie, S. Highly Stretchable Integrated System for Micro–Supercapacitor with AC Line Filtering and UV Detector. *Nano Energy* **2017**, *42*, 187–194.

(3) Guo, R.; Chen, J.; Yang, B.; Liu, L.; Su, L.; Shen, B.; Yan, X. In–Plane Micro–Supercapacitors for an Integrated Device on One Piece of Paper. *Adv. Funct. Mater.* **2017**, *27*, 1702394.

(4) Song, Y.; Chen, H.; Su, Z.; Chen, X.; Miao, L.; Zhang, J.; Cheng, X.; Zhang, H. Highly Compressible Integrated Supercapacitor–Piezoresistance–Sensor System with CNT–PDMS Sponge for Health Monitoring. *Small* **2017**, *13*, 1702091.

(5) Chen, C.; Cao, J.; Lu, Q.; Wang, X.; Song, L.; Niu, Z.; Chen, J. Foldable All–Solid–State Supercapacitors Integrated with Photodetectors. *Adv. Funct. Mater.* **2017**, *27*, 1604639.

(6) Lou, Z.; Li, L.; Wang, L.; Shen, G. Recent Progress of Self–Powered Sensing Systems for Wearable Electronics. *Small* **2017**, *13*, 1701791.

(7) Yun, J.; Lim, Y.; Jang, G. N.; Kim, D.; Lee, S.; Park, H.; Hong, Y. S.; Lee, G.; Zi, G.; Ha, J. S. Stretchable Patterned Graphene Gas Sensor Driven by Integrated Micro–Supercapacitor Array. *Nano Energy* **2016**, *19*, 401–414.

(8) Aytug, T.; Rager, M. S.; Higgins, W.; Brown, F. G.; Veith, G. M.; Rouleau, C. M.; Wang, H.; Hood, Z. D.; Mahurin, S. M.; Mayes, R. T.; et al. Vacuum–Assisted Low–Temperature Synthesis of Reduced Graphene Oxide Thin–Film Electrodes for High–Performance Transparent and Flexible All–Solid–State Supercapacitors. *ACS Appl. Mater. Interfaces* **2018**, *10*, 11008–11017.

(9) Zhang, Y.; Bai, W.; Cheng, X.; Ren, J.; Weng, W.; Chen, P.; Fang, X.; Zhang, Z.; Peng, H. Flexible and Stretchable Lithium–Ion Batteries and Supercapacitors Based on Electrically Conducting Carbon Nanotube Fiber Springs. *Angew. Chemie–Int. Ed.* **2014**, *53*, 14564–14568.

(10) Wang, J.; Jin, D.; Zhou, R.; Li, X.; Liu, X.; Shen, C.; Xie, K.; Li, B.; Kang, F.; Wei, B. Highly Flexible Graphene/Mn_3O_4 Nanocomposite Membrane as Advanced Anodes for Li–Ion Batteries. *ACS Nano* **2016**, *10*, 6227–6234.

(11) Yu, S.; Schmohl, S.; Liu, Z.; Hoffmeyer, M.; Schön, N.; Hausen, F.; Tempel, H.; Kungl, H.; Wiemhöfer, H.; Eichel, R. Insights into a Layered Hybrid Solid Electrolyte and Its Application in Long Lifespan High–Voltage All–Solid–State Lithium Batteries. *J. Mater. Chem. A* **2019**, *7*, 3882–3894.

(12) Cao, C.; Li, Z.–B.; Wang, X.–L.; Zhao, X.–B.; Han, W.–Q. Recent Advances in Inorganic Solid Electrolytes for Lithium Batteries. *Front. Energy Res.* **2014**, *2*, 00025.

(13) Yu, S.; Liu, Z.; Tempel, H.; Kungl, H.; Eichel, R. Self–Standing NASICON–Type Electrodes with High Mass Loading for Fast Cycling Flexible All–Phosphate Sodium–Ion Batteries. *J. Mater. Chem. A* **2018**, *6*, 18304–18317.

(14) Yu, S.; Mertens, A.; Tempel, H.; Schierholz, R.; Kungl, H.; Eichel, R. Monolithic All–Phosphate Solid–State Lithium–Ion Battery with Improved Interfacial Compatibility. *ACS Appl. Mater. Interfaces* **2018**, 22264–22277.

(15) Yao, M.; Wang, R.; Zhao, Z.; Liu, Y.; Niu, Z.; Chen, J. A Flexible All–in–One Lithium–Sulfur Battery. *ACS Nano* **2018**, *12*, 12503–12511.

(16) Wang, Q.; Ping, P.; Zhao, X.; Chu, G.; Sun, J.; Chen, C. Thermal Runaway Caused Fire and Explosion of Lithium Ion Battery. *J. Power Sources* **2012**, *208*, 210–224.

(17) Liu, N.; Lu, Z.; Zhao, J.; Mcdowell, M. T.; Lee, H.; Zhao, W; Cui, Y. A Pomegranate–Inspired Nanoscale Design for Large–Volume–Change Lithium Battery Anodes. *Nat. Nanotechnol.* **2014**, *9*,187–192.

(18) Xu, J.; Lin, F.; Doeff, M. M.; Tong, W. A Review of Ni–Based Layered Oxides for Rechargeable Li–Ion Batteries. *J. Mater. Chem. A* **2017**, *5*, 874–901.

(19) Liu, L.; Song, T.; Han, H.; Park, H.; Xiang, J.; Liu, Z.; Feng, Y.; Paik, U. Electrospun Sn–Doped $LiTi_{2(}PO_4)_3$/C Nanofibers for Ultra–Fast Charging and Discharging. *J. Mater. Chem. A* **2015**, *3*, 10395–10402.

(20) Wang, H.; Zhang, H.; Cheng, Y.; Feng, K.; Li, X.; Zhang, H. Rational Design and Synthesis of $LiTi_2(PO_4)_{3-x}F_x$ Anode Materials for High–Performance Aqueous Lithium Ion Batteries. *J. Mater. Chem. A* **2017**, *5*, 593–599.c

(21) Yuan, W.; Yan, J.; Tang, Z.; Sha, O.; Wang, J.; Mao, W.; Ma, L. Mo–Doped $Li_3V_2(PO_4)_3$/C Cathode Material with High Rate Capability and Long Term Cyclic Stability. *Electrochim. Acta* **2012**, *72*, 138–142.

(22) Son, J. N.; Kim, S. H.; Kim, M. C.; Kim, G. J.; Aravindan, V.; Lee, Y. G.; Lee, Y. S. Electrochimica Acta Superior Charge–Transfer Kinetics of NASICON–Type $Li_3V_2(PO_4)_3$ Cathodes by Multivalent Al^{3+} and Cl^- Substitutions. *Electrochim. Acta* **2013**, *97*, 210–215.

(23) Yue, S.; Tong, H.; Lu, L.; Tang, W.; Bai, W.; Jin, F.; Han, Q.; He, J.; Liu, J.; Zhang, X. Hierarchical $NiCo_2O_4$ Nanosheets/Nitrogen Doped Graphene/Carbon Nanotube Film with Ultrahigh Capacitance and Long Cycle Stability as a Flexible Binder–Free Electrode for Supercapacitors. *J. Mater. Chem. A* **2017**, *5*, 689–698.

(24) Rui, X.; Sun, W.; Wu, C.; Yu, Y.; Yan, Q. An Advanced Sodium–Ion Battery Composed of Carbon Coated $Na_3V_2(PO_4)_3$ in a Porous Graphene Network. *Adv. Mater.* **2015**, *27*, 6670–6676.

(25) Yehezkel, S.; Auinat, M.; Sezin, N.; Starosvetsky, D.; Ein–eli, Y. Bundled and Densified Carbon Nanotubes (CNT) Fabrics as Flexible Ultra–Light Weight Li–Ion Battery Anode Current Collectors. *J. Power Sources* **2016**, *312*, 109–115.

(26) Wang, W.; Xu, Q.; Liu, H.; Wang, Y.; Xia, Y. A Flexible Symmetric Sodium Full Cell Constructed Using the Bipolar Material $Na_3V_2(PO_4)_3$. *J. Mater. Chem. A* **2017**, *5*, 8440–8450.

(27) David, L.; Bhandavat, R.; Singh, G. MoS_2/Graphene Composite Paper for Sodium–Ion Battery Electrodes. *ACS Nano* **2014**, *8*, 1759–1770.

(28) Pan, Z.; Ren, J.; Guan, G.; Fang, X.; Wang, B.; Doo, S.; Son, H.; Huang, X.; Peng, H. Synthesizing Nitrogen–Doped Core–Sheath Carbon Nanotube Films for Flexible Lithium Ion Batteries. *Adv. Energy Mater.* **2016**, *6*, 1600271.

(29) Zhang, Z.; Xiao, F.; Qian, L.; Xiao, J.; Wang, S.; Liu, Y. Facile Synthesis of 3D MnO_2–Graphene and Carbon Nanotube–Graphene Composite Networks for High– Performance, Flexible, All–Solid–State Asymmetric Supercapacitors. *Adv. Energy Mater.* **2014**, *4*, 1400064.

(30) Jing, M.; Zhai, H.; Pi, Z.; Li, J.; Chen, L.; Shen, X.; Xi, X.; Xiao, K. High Loading $LiFePO_4$ on Activated Carbon Fiber Cloth as a High Capacity Cathode for Li–Ion Battery. *Russ. J. Appl. Chem.* **2016**, *89*, 1183–1188.

(31) Zhu, Y.; He, X.; Mo, Y. Origin of Outstanding Stability in the Lithium Solid Electrolyte Materials : Insights from Thermodynamic Analyses Based on First– Principles Calculations. *ACS Appl. Mater. Interfaces* **2015**, *7*, 23685–23693.

(32) Zhou, D.; Shanmukaraj, D.; Tkacheva, A.; Armand, M.; Wang, G. Polymer Electrolytes for Lithium–Based Batteries : Advances and Prospects. *Chem* **2019**, *5*, 2326–2352.

(33) Zheng, F.; Kotobuki, M.; Song, S.; Lai, M. O.; Lu, L. Review on Solid Electrolytes for All–Solid–State Lithium–Ion Batteries. *J. Power Sources* **2018**, *389*, 198–213.

(34) Blonsky, P. M.; Shriver, D. F. Polyphosphazene Solid Electrolyte. *J. Am. Chem. Soc.* **1984**, *106*, 6854–6855.

(35) Jankowsky, S.; Hiller, M. M.; Wiemhöfer, H. Preparation and Electrochemical Performance of Polyphosphazene Based Salt–in–Polymer Electrolyte Membranes for Lithium Ion Batteries. *J. Power Sources* **2014**, *253*, 256–262.

(36) Jankowsky, S.; Hiller, M. M.; Fromm, O.; Winter, M.; Wiemhöfer, H. Enhanced Lithium–Ion Transport in Polyphosphazene Based Gel Polymer Electrolytes. *Electrochim. Acta* **2015**, *155*, 364–371.

(37) Allcock, H. R. Polyphosphazene Elastomers, Gels, and Other Soft Materials. *Soft Matter* **2012**, *8*, 7521–7532.

(38) Paulsdorf, J.; Kaskhedikar, N.; Burjanadze, M.; Obeidi, S.; Stolwijk, N. A.; Wilmer, D.; Wiemhöfer, H. Synthesis and Ionic Conductivity of Polymer Electrolytes Based on a Polyphosphazene with Short Side Groups. *Chem. Mater.* **2006**, *18*, 1281–1288.

(39) Santhanagopalan, D.; Qian, D.; Mcgilvray, T.; Wang, Z.; Wang, F.; Camino, F.; Graetz, J.; Dudney, N.; Meng, Y. S. Interface Limited Lithium Transport in Solid–State Batteries. *J. Phys. Chem. Lett.* **2014**, *5*, 298–303.

(40) Wang, Z.; Santhanagopalan, D.; Zhang, W.; Wang, F.; Xin, H. L.; He, K.; Li, J.; Dudney, N.; Meng, Y. S. In Situ STEM–EELS Observation of Nanoscale Interfacial Phenomena in All–Solid–State Batteries. *Nano Lett.* **2016**, *16*, 3760–3767.

(41) Takada, K. Interfacial Nanoarchitectonics for Solid–State Lithium Batteries. *Langmuir* **2013**, *29*, 7538–7541.

(42) Jung, Y. S.; Oh, D. Y.; Nam, Y. J.; Park, K. H. Issues and Challenges for Bulk–Type All–Solid–State Rechargeable Lithium Batteries Using Sulfide Solid Electrolytes. *Isr. J. Chem.* **2015**, *55*, 472–485.

(43) Han, F.; Gao, T.; Zhu, Y.; Gaskell, K. J.; Wang, C. A Battery Made from a Single Material. *Adv. Mater.* **2015**, *27*, 3473–3483.

(44) McGuire K.; Rao, A. M. *Characterization Techniques in Carbon Nanotube Research. In Carbon Nanotubes: Science and Applications*; CRC Press LLC: Boca Raton, US, **2004**, pp133–134.

(45) Dresselhaus, M. S.; Jorio, A.; Saito, R. Characterizing Graphene, Graphite, and Carbon Nanotubes by Raman Spectroscopy. *Annu. Rev. Condens. Matter Phys.* **2010**, *1*, 89–108.

(46) Hossain, M. M.; Shima, H.; Islam, A.; Hasan, M.; Lee, M. Synergetic Effect in Raman Scattering of ZnO Nanoparticles in ZnO−CNT Fibers : A Way To Enhance the G and 2D Band. *J. Phys. Chem. C* **2016**, *120*, 17670–17682.

(47) Guo, D.; Qin, J.; Yin, Z.; Bai, J.; Sun, Y.; Cao, M. Achieving High Mass Loading of $Na_3V_2(PO_4)_3$@Carbon on Carbon Cloth by Constructing Three–Dimensional Network Between Carbon Fibers for Ultralong Cycle–Life and Ultrahigh Rate Sodium–Ion Batteries. *Nano Energy* **2018**, *45*, 136–147.

(48) Ren, W.; Zhou, W.; Zhang, H.; Cheng, C. ALD TiO_2–Coated Flower–like MoS_2 Nanosheets on Carbon Cloth as Sodium Ion Battery Anode with Enhanced Cycling Stability and Rate Capability. *ACS Appl. Mater. Interfaces* **2017**, *9*, 487–495.

(49) Ren, W.; Zhang, H.; Guan, C.; Cheng, C. Ultrathin MoS_2 Nanosheets@Metal Organic Framework– Derived N–Doped Carbon Nanowall Arrays as Sodium Ion Battery Anode with Superior Cycling Life and Rate Capability. *Adv. Funct. Mater.* **2017**, *27*, 1702116.

(50) Yu, S.; Tempel, H.; Schierholz, R.; Aslanbas, Ö.; Gao, X.; Mertens, J.; de Haart, L. G. J.; Kungl, H.; Eichel, R.–A. $LiTi_2(PO_4)_3$/C Anode Material with a Spindle–Like Morphology for Batteries with High Rate Capability and Improved Cycle Life. *ChemElectroChem* **2016**, *3*, 1157–1169.

(51) Zhao, B.; Wang, Q.; Zhang, S.; Deng, C. Self–Assembled Wafer–like Porous $NaTi_2(PO_4)_3$ Decorated with Hierarchical Carbon as a High–Rate Anode for Aqueous Rechargeable Sodium Batteries. *J. Mater. Chem. A* **2015**, *3*, 12089–12096.

(52) Yu, S.; Mertens, A.; Kungl, H.; Schierholz, R.; Tempel, H.; Eichel, R.–A. Morphology Dependency of $Li_3V_2(PO_4)_3$/C Cathode Material Regarding to Rate Capability and Cycle Life in Lithium–Ion Batteries. *Electrochim. Acta* **2017**, *232*, 310–322.

(53) Zhang, Y.; Qiu, C.; Li, Y.; Zhang, W.; Wang, X. Synthesis and Characterization of a New Type of Electro–Optic Polymer without Carbon Main Chains. *Mater. Sci. Pol.* **2014**, *32*, 402–407.

(54) Online, V. A.; Yesappa, L.; Niranjana, M.; Vijeth, H.; Basappa, M.; Dwivedi, J.; Petwal, V. C.; Ganesh, S.; Devendrappa, H. Optical Properties and Ionic Conductivity Studies of an 8 MeV Electron Beam Irradiated Poly(vinylidene fluoride–*co*–hexafluoropropylene)/$LiClO_4$ Electrolyte Film for Opto–Electronic Applications. *RSC Adv.* **2018**, *8*, 15297–15309.

(55) Stephan, A. M.; Nahm, K. S. Review on Composite Polymer Electrolytes for Lithium Batteries. *Polymer (Guildf).* **2006**, *47*, 5952–5964.

(56) Yu, S.; Chen, L.; Chen, Y.; Tong, Y. Applied Surface Science Microporous Gel Electrolytes Based on Amphiphilic Poly(vinylidene fluoride–*co*–hexafluoropropylene) for Lithium Batteries. *Appl. Surf. Sci.* **2012**, *258*, 4983–4989.

(57) Bobade, R. S.; Yawale, S. V. P.; Yawale, S. P. Electrical Investigation of Polythiophene–Poly (Vinyl Acetate) Composite Films via VTF and Impedance Spectroscopy. *J. Non. Cryst. Solids* **2009**, *355*, 2410–2414.

(58) Baskaran, R.; Selvasekarapandian, S.; Kuwata, N.; Kawamura, J.; Hattori, T. Ac Impedance, DSC and FT–IR Investigations on (x)PVAc–(1−x) PVdF Blends with $LiClO_4$. *Mater. Chem. Phys.* **2006**, *98*, 55–61.

(59) Aziz, S. B.; Woo, T. J.; Kadir, M. F. Z.; Ahmed, H. M. A Conceptual Review on Polymer Electrolytes and Ion Transport Models. *J. Sci. Adv. Mater. Devices* **2018**, *3*, 1–17.

(60) Liu, Z.; Qin, X.; Xu, H.; Chen, G. One–Pot Synthesis of Carbon–Coated Nanosized $LiTi_2(PO_4)_3$ as Anode Materials for Aqueous Lithium Ion Batteries. *J. Power Sources* **2015**, *293*, 562–569.

(61) Sun, D.; Xue, X.; Tang, Y.; Jing, Y.; Huang, B.; Ren, Y.; Yao, Y.; Wang, H.; Cao, G. High–Rate $LiTi_2(PO_4)_3$@N−C Composite via Bi–nitrogen Sources Doping. *ACS Appl. Mater. Interfaces* **2015**, *7*, 28337–28345.

(62) Wei, Q.; An, Q.; Chen, D.; Mai, L.; Chen, S.; Zhao, Y. One–Pot Synthesized Bicontinuous Hierarchical $Li_3V_2(PO_4)_3$/C Mesoporous Nanowires for High–Rate and Ultralong–Life Lithium–Ion Batteries. *Nano Lett.* **2014**, *14*, 1042–1048.

(63) Dahn, J. R.; Zheng, T.; Liu, Y.; Xue, J. S. Mechanisms for Lithium Insertion in Carbonaceous Materials. *Science* **1995**, *270*, 590–593.

(64) Yang, Z.; Wu, H. Electrochemical Intercalation of Lithium into Carbon Nanotubes. *Solid State Ionics* **2001**, *143*, 173–180.

(65) Chen, S.; Shen, L.; van Aken, P. A.; Maier, J.; Yu, Y. Dual–Functionalized Double Carbon Shells Coated Silicon Nanoparticles for High Performance Lithium–Ion Batteries. *Adv. Mater.* **2017**, *29*, 1605650.

(66) Ma, S.; Jiang, M.; Tao, P.; Song, C.; Wu, J.; Wang, J. Materials International Temperature Effect and Thermal Impact in Lithium–Ion Batteries : A Review. *Prog. Nat. Sci. Mater. Int.* **2018**, *28*, 653–666.

(67) Bard, A.; Faulkner, L. R. *Electrochemical Methods*, Wiley press: New York, US, **2001**, pp156–225.

(68) Yang, X.; Zhang, G.; Ge, S.; Wang, C. Fast Charging of Lithium–Ion Batteries at All Temperatures. *Proc. Natl. Acad. Sci. U.S.A.* **2018**, *115*, 7266–7271.

(69) Leng, F.; Tan, C. M.; Pecht, M. Effect of Temperature on the Aging Rate of Li Ion Battery Operating above Room Temperature. *Sci. Rep.* **2015**, *5*, 12967.

(70) Laidler, K. J. The Development of the Arrhenius Equation. *J. Chem. Educ.* **1984**, *61*, 494–498.

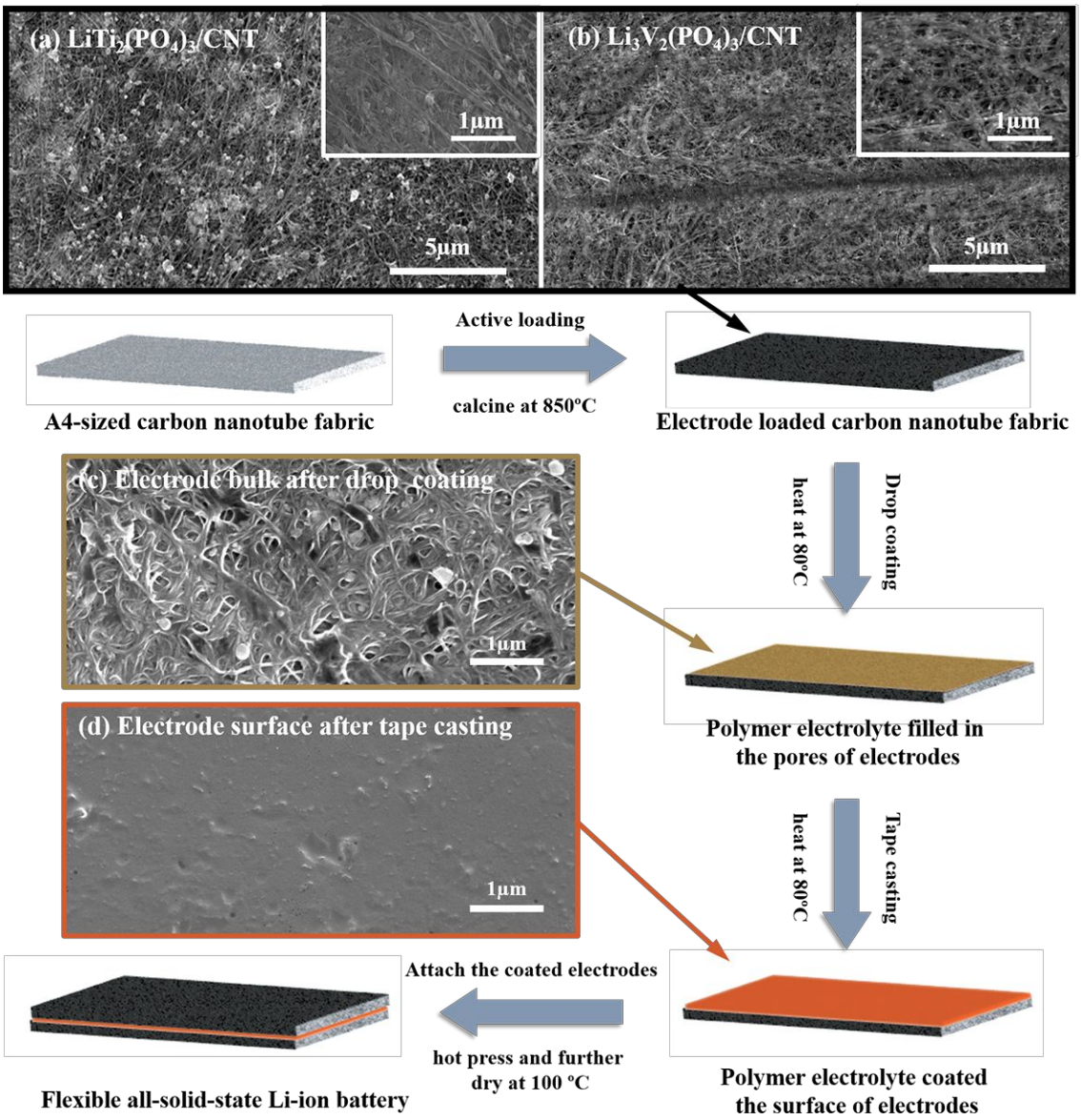

Figure 1. Illustration of the preparation steps of self–standing $LiTi_2(PO_4)_3$/CNT, $Li_3V_2(PO_4)_3$/CNT and flexible all–solid–state battery. The SEM images were recorded for as–prepared electrodes ((a) and (b)), polymer drop coated (c) and polymer tape casted (d) self–standing electrodes, respectively. The SEM images after polymer coating/casting were recorded for $LiTi_2(PO_4)_3$/CNT electrode for demonstration as the microstructure is the same for $Li_3V_2(PO_4)_3$/CNT.

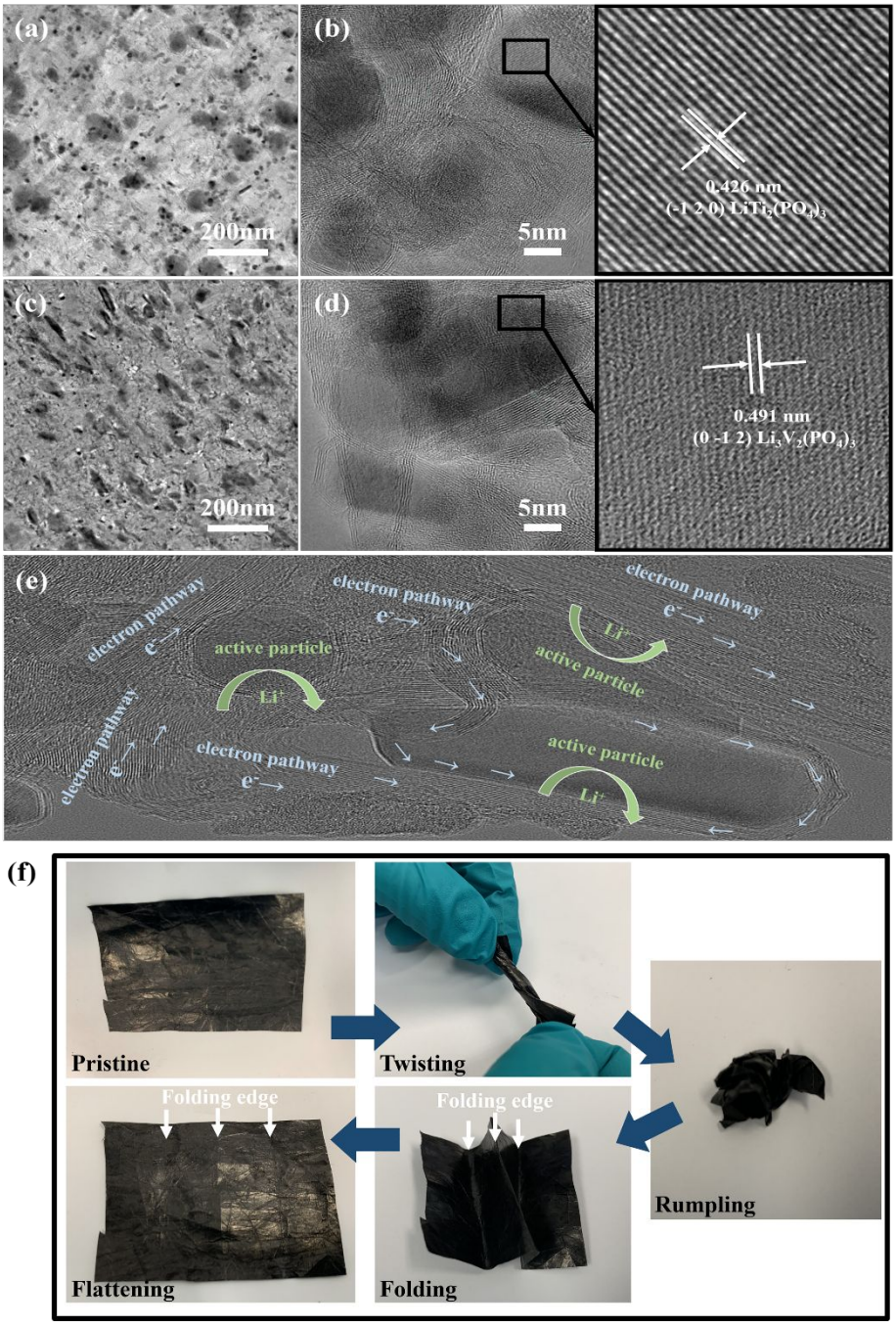

Figure 2. TEM and HR–TEM images of $LiTi_2(PO_4)_3$/CNT ((a) and (b)) and $Li_3V_2(PO_4)_3$/CNT ((c)–(d)). (e) Possible Li^+ and electron pathways in the self–standing electrodes. (f) Visual inspection of the self–standing electrodes after twisting, rumpling and folding. Figure 2 (e) and (f) are using $LiTi_2(PO_4)_3$/CNT electrode for the demonstration as the electrodes exhibit similar morphology and mechanical property.

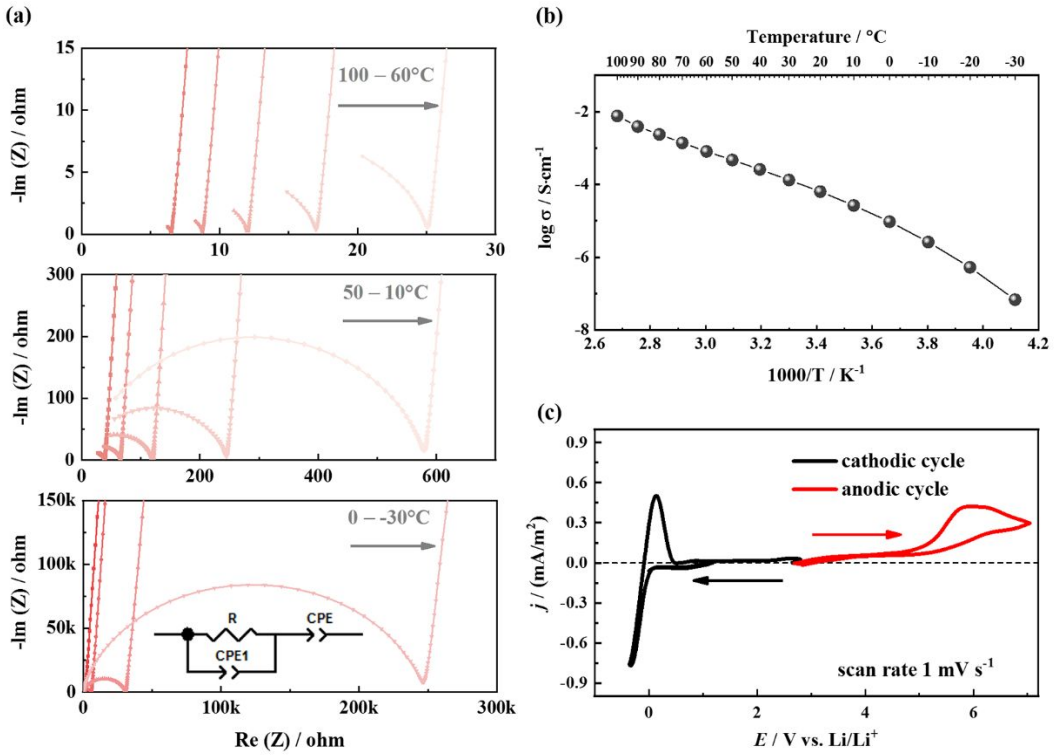

Figure 3. Experimental Nyquist plot of the impedance spectra (a) and Arrhenius plot (b) of the solid polymer electrolyte in a temperature range of –30 to 100 °C. The impedance spectra was measured with gold coated Cu electrodes. And cyclic voltammetry curve (c) of the solid polymer electrolyte with a scan rate of 1 mV s^{-1} at 30 °C. The anodic oxidation limit was measured in the range from 2.6 V to 7.0 V using an inert polarizable platinum working electrode. The cathodic reduction limit was determined analogously between 2.8 V and –0.4 V by choosing an inert copper electrode as polarizable working electrode.

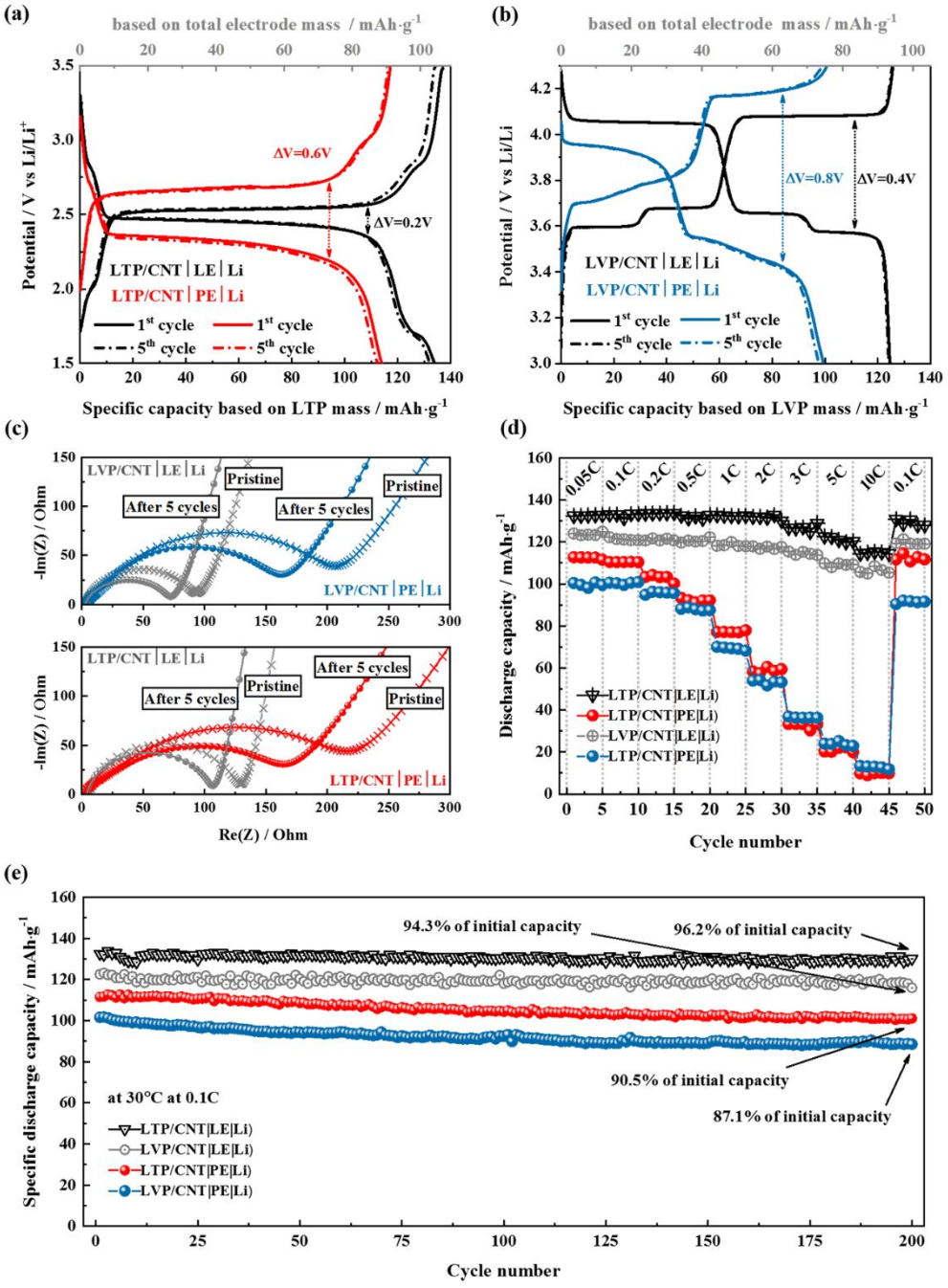

Figure 4. Electrochemical performance of $LiTi_2(PO_4)_3$/CNT and $Li_3V_2(PO_4)_3$/CNT electrodes in half–cells (*vs* metallic lithium) with liquid electrolyte (LE) and solid polymer electrolyte (PE), respectively. Charge–discharge profiles of first and fifth cycles at 0.05C after one formation cycle ((a) and (b)). (c) Nyquist plot before and after the five cycles at 0.05C. Rate performance and cycling performance at 0.1C ((d) and (e)). All the electrochemical measurements were performed at 30 °C. Red and blue symbols correlate to the results obtained from $LiTi_2(PO_4)_3$/CNT and $Li_3V_2(PO_4)_3$/CNT half–cells with polymer electrolyte, respectively. Black and grey colored symbols indicating the performance of half–cells with liquid electrolyte.

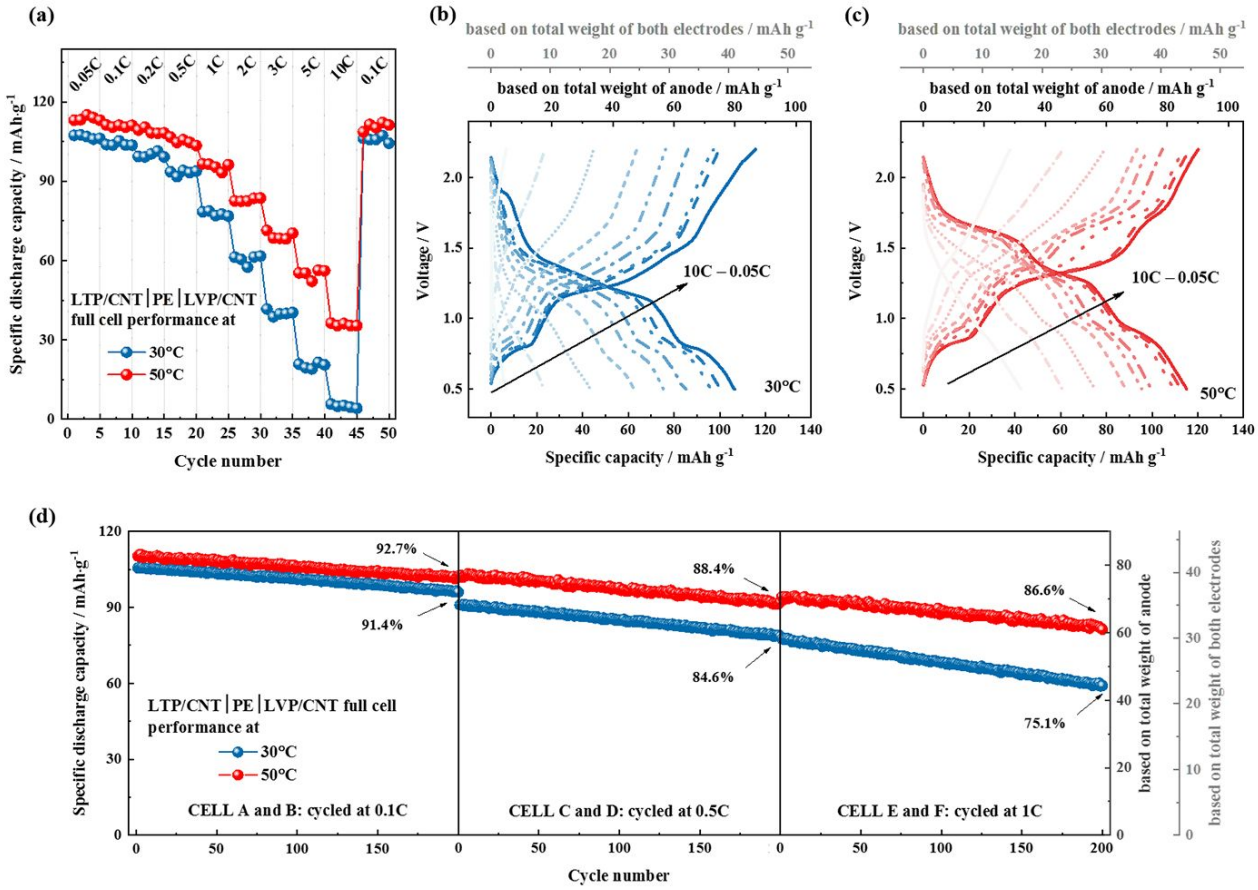

Figure 5. Electrochemical performance of $LiTi_2(PO_4)_3$/CNT|MEEP/PVDF–HFP/LiBOB polymer electrolyte (PE)|$Li_3V_2(PO_4)_3$/CNT full cells. Rate performance (a) and corresponding charge–discharge profiles at 30 and 50 °C, respectively ((b) and (c)). Cycling stability of two cells each at the current rates of 0.1C, 0.5C and 1C at different temperatures of 30 and 50 °C, respectively (d).

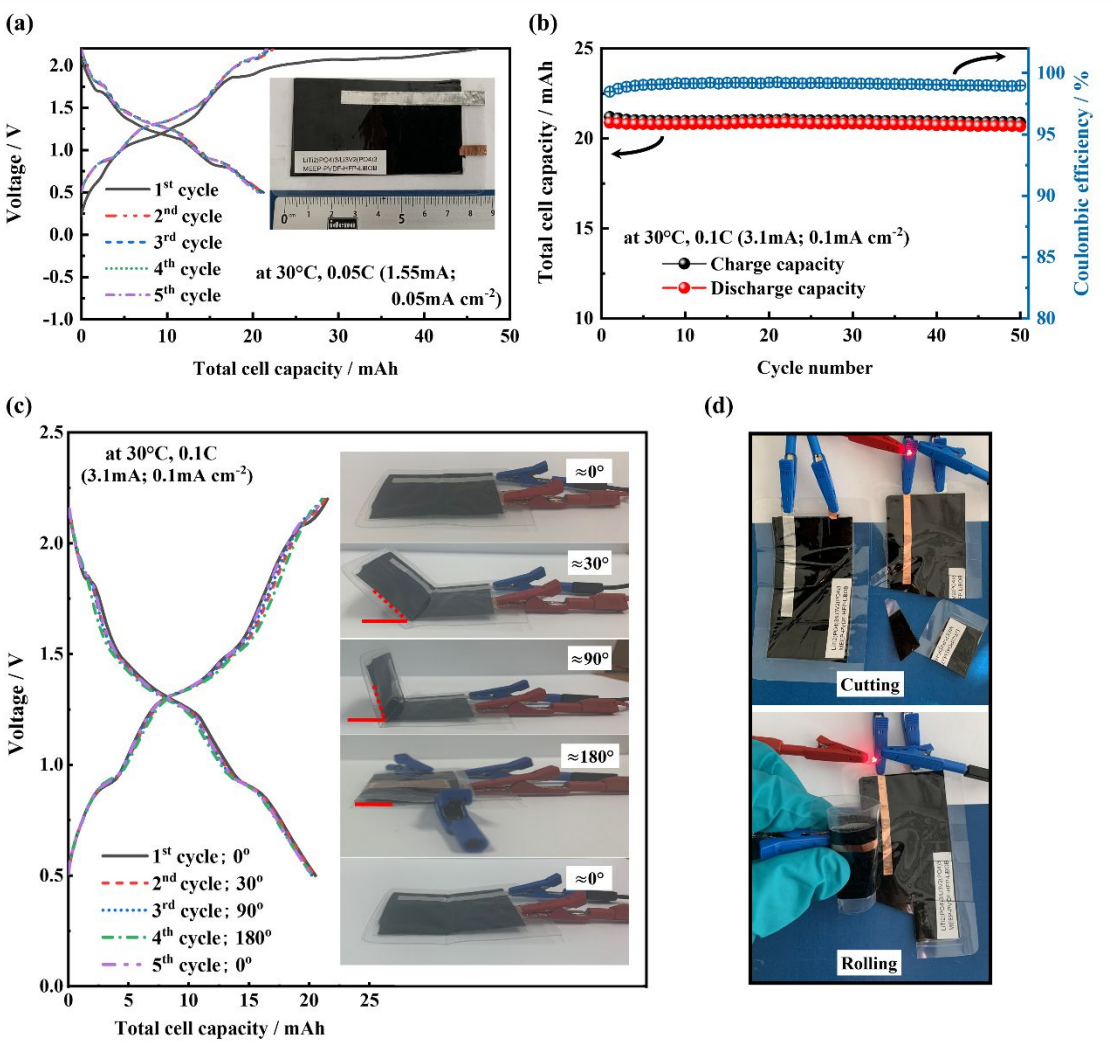

Figure 6. (a) Charge–discharge profiles at 0.05C (1.55 mA) and photographs of $LiTi_2(PO_4)_3$/CNT|MEEP/PVDF–HFP/LiBOB polymer electrolyte|$Li_3V_2(PO_4)_3$/CNT prototype flexible laminated cell after formation and long–term cycling. (b) Cycling stability of the battery at 0.1C (3.2 mA). (c) Charge–discharge curves of the folded cell at different angles at 1C. (d) Photographs of cutting and rolling tests during battery operation. The red LED was powered by two charged flexible all–phosphate solid–state Li–ion batteries connected in series.

TABLE OF CONTENTS

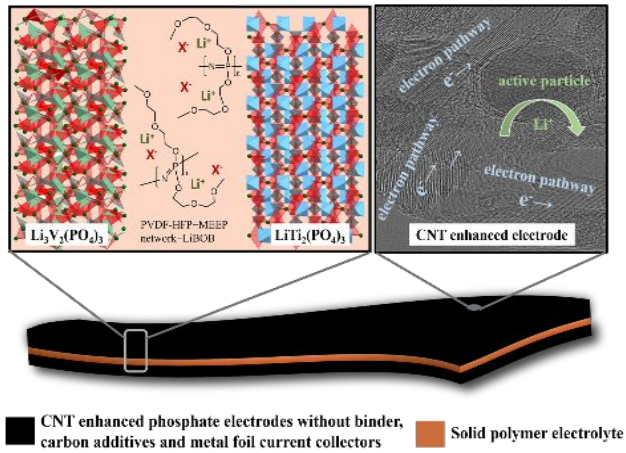

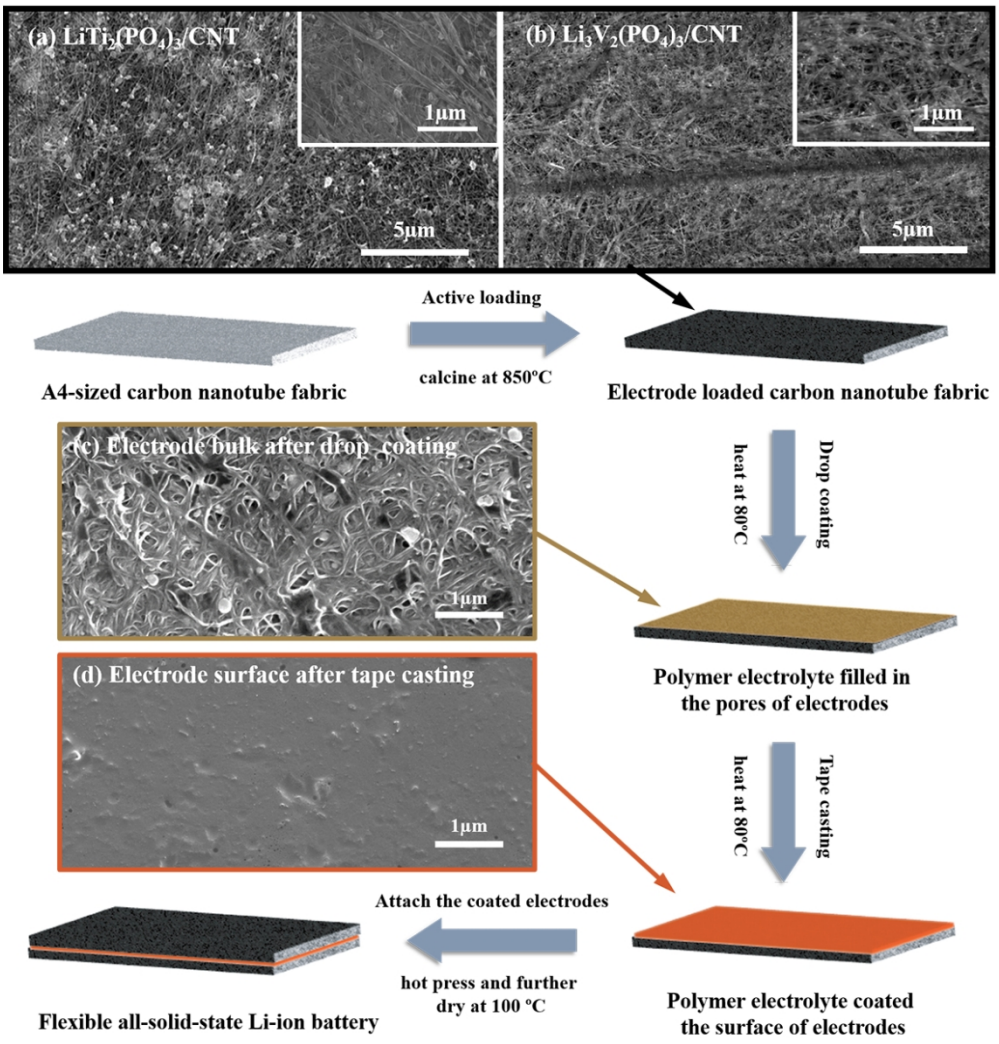

Figure 1. Illustration of the preparation steps of self–standing $LiTi_2(PO_4)_3$/CNT, $Li_3V_2(PO_4)_3$/CNT and flexible all–solid–state battery. The SEM images were recorded for as–prepared electrodes ((a) and (b)), polymer drop coated (c) and polymer tape casted (d) self–standing electrodes, respectively. The SEM images after polymer coating/casting were recorded for $LiTi_2(PO_4)_3$/CNT electrode for demonstration as the microstructure is the same for $Li_3V_2(PO_4)_3$/CNT.

99x104mm (300 x 300 DPI)

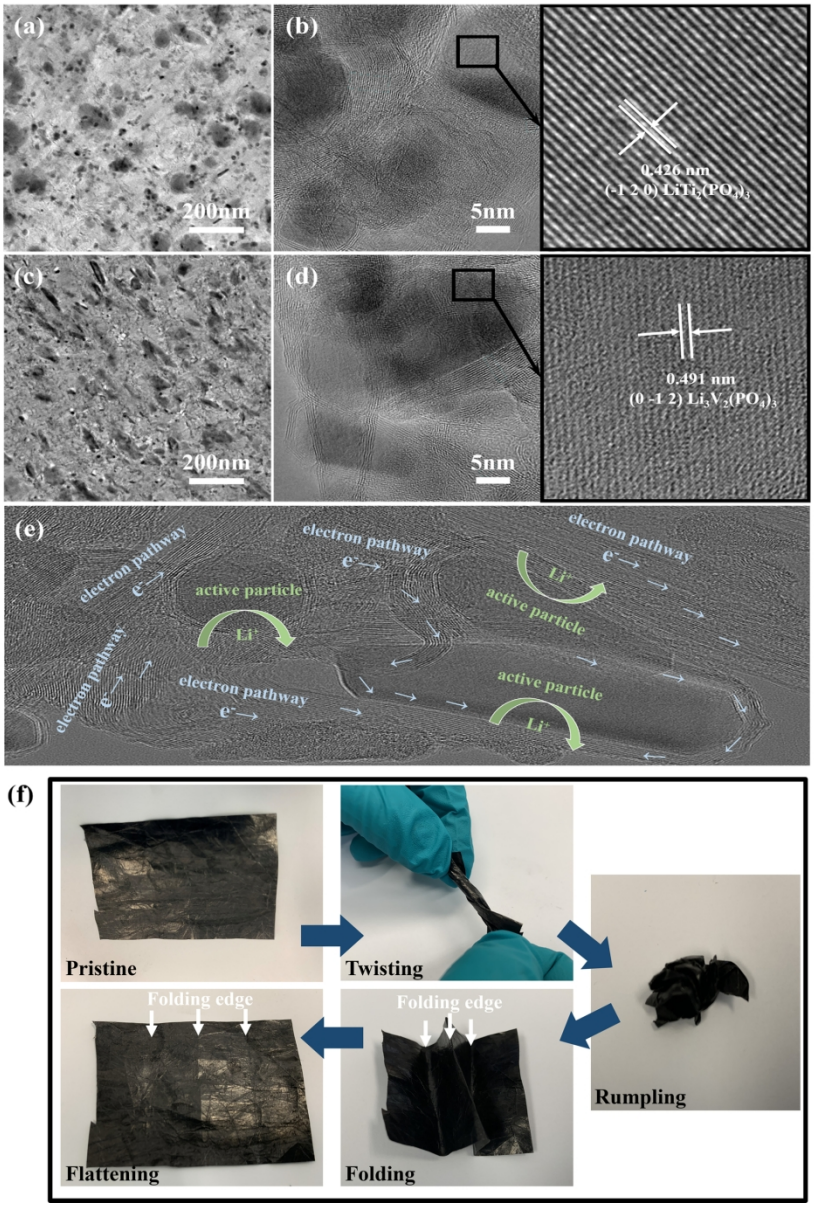

Figure 2. TEM and HR–TEM images of $LiTi_2(PO_4)_3$/CNT ((a) and (b)) and $Li_3V_2(PO_4)_3$/CNT ((c)–(d)). (e) Possible Li+ and electron pathways in the self–standing electrodes. (f) Visual inspection of the self–standing electrodes after twisting, rumpling and folding. Figure 2 (e) and (f) are using $LiTi_2(PO_4)_3$/CNT electrode for the demonstration as the electrodes exhibit similar morphology and mechanical property.

149x215mm (300 x 300 DPI)

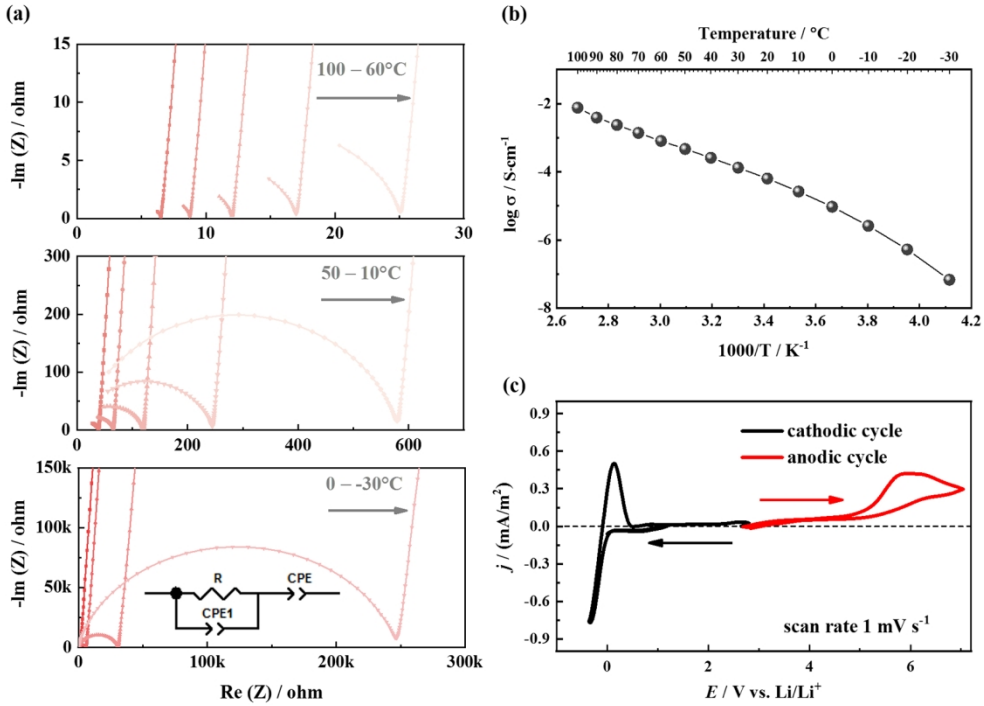

Figure 3. Experimental Nyquist plot of the impedance spectra (a) and Arrhenius plot (b) of the solid polymer electrolyte in a temperature range of −30 to 100 °C. The impedance spectra was measured with gold coated Cu electrodes. And cyclic voltammetry curve (c) of the solid polymer electrolyte with a scan rate of 1 mV s^{-1} at 30 °C. The anodic oxidation limit was measured in the range from 2.6 V to 7.0 V using an inert polarizable platinum working electrode. The cathodic reduction limit was determined analogously between 2.8 V and −0.4 V by choosing an inert copper electrode as polarizable working electrode.

150x106mm (300 x 300 DPI)

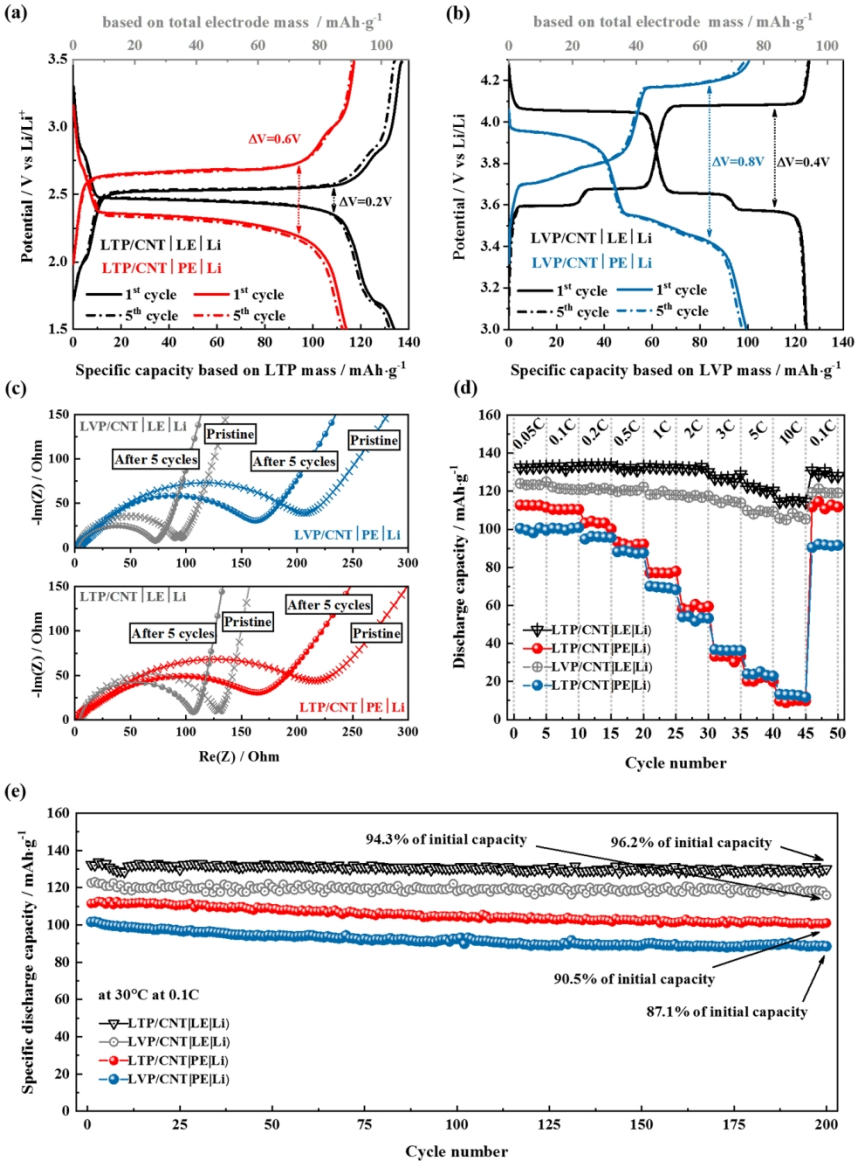

Figure 4. Electrochemical performance of $LiTi_2(PO_4)_3$/CNT and $Li_3V_2(PO_4)_3$/CNT electrodes in half–cells (vs metallic lithium) with liquid electrolyte (LE) and solid polymer electrolyte (PE), respectively. Charge–discharge profiles of first and fifth cycles at 0.05C after one formation cycle ((a) and (b)). (c) Nyquist plot before and after the five cycles at 0.05C. Rate performance and cycling performance at 0.1C ((d) and (e)). All the electrochemical measurements were performed at 30 °C. Red and blue symbols correlate to the results obtained from $LiTi_2(PO_4)_3$/CNT and $Li_3V_2(PO_4)_3$/CNT half–cells with polymer electrolyte, respectively. Black and grey colored symbols indicating the performance of half–cells with liquid electrolyte.

122x160mm (300 x 300 DPI)

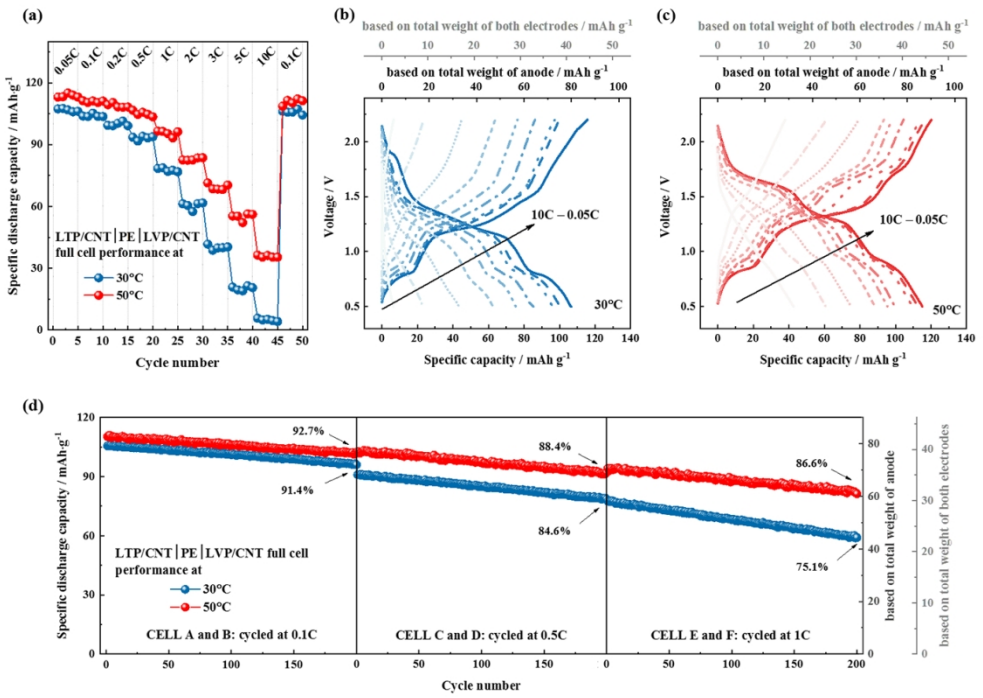

Figure 5. Electrochemical performance of $LiTi_2(PO_4)_3$/CNT|MEEP/PVDF–HFP/LiBOB polymer electrolyte (PE)|$Li_3V_2(PO_4)_3$/CNT full cells. Rate performance (a) and corresponding charge–discharge profiles at 30 and 50 °C, respectively ((b) and (c)). Cycling stability of two cells each at the current rates of 0.1C, 0.5C and 1C at different temperatures of 30 and 50 °C, respectively (d).

119x84mm (300 x 300 DPI)

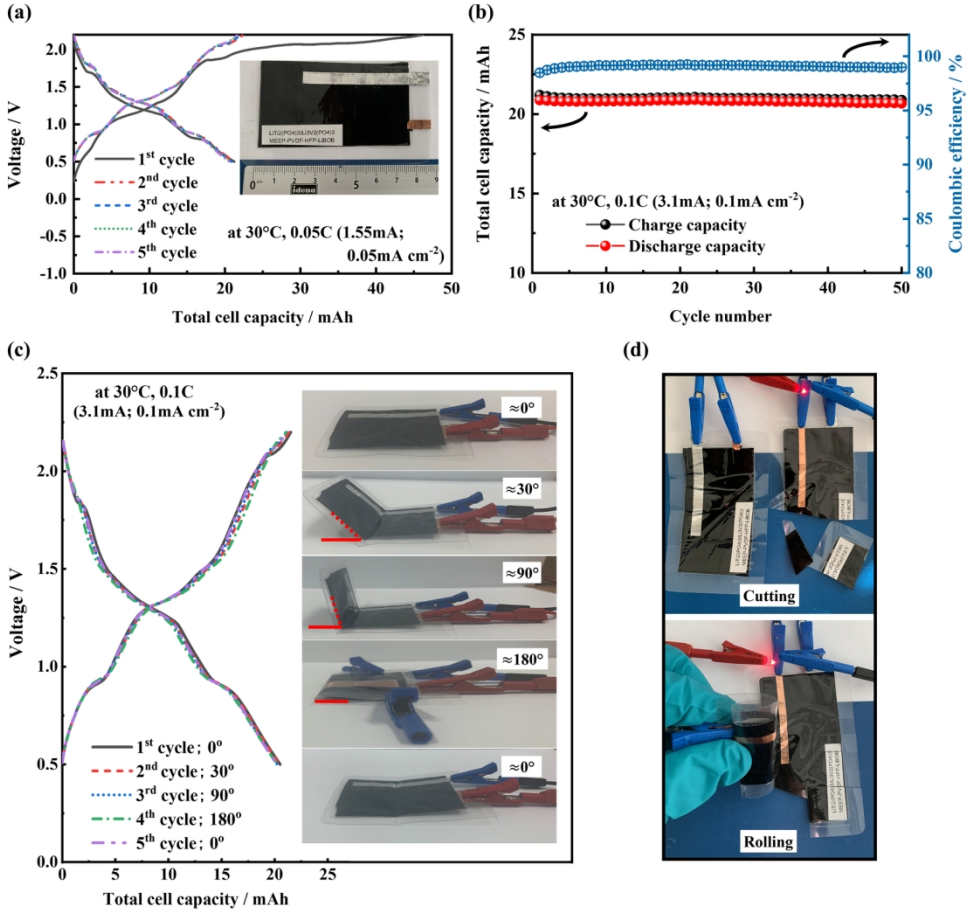

Figure 6. (a) Charge–discharge profiles at 0.05C (1.55 mA) and photographs of $LiTi_2(PO_4)_3$/CNT|MEEP/PVDF–HFP/LiBOB polymer electrolyte|$Li_3V_2(PO_4)_3$/CNT prototype flexible laminated cell after formation and long–term cycling. (b) Cycling stability of the battery at 0.1C (3.2 mA). (c) Charge–discharge curves of the folded cell at different angles at 1C. (d) Photographs of cutting and rolling tests during battery operation. The red LED was powered by two charged flexible all–phosphate solid–state Li–ion batteries connected in series.

149x139mm (300 x 300 DPI)